Spring 2007

Band Gap Engineering of Two Dimensional Silicon Photonic Crystals by Oxidation and Oxide Etching

Makhin Thitsa
Old Dominion University

BAND GAP ENGINEERING OF TWO DIMENSIONAL SILICON PHOTONIC CRYSTALS BY OXIDATION AND OXIDE ETCHING

by

Makhin Thitsa
B.S.E.E. August 2005, Old Dominion University

A Thesis Submitted to the Faculty of
Old Dominion University in Partial Fulfillment of the
Requirements for the Degree of

MASTER OF SCIENCE

ELECTRICAL ENGINEERING

OLD DOMINION UNIVERSITY
May 2007

Approved by:

Sacharia Albin (Director)

K. Vijayan Asari (Member)

Helmut Baumgart (Member)

ABSTRACT

BAND GAP ENGINEERING OF TWO DIMENSIONAL SILICON PHOTONIC CRYSTALS BY OXIDATION AND OXIDE ETCHING

Makhin Thitsa
Old Dominion University, May 2007
Director: Dr. Sacharia Albin

In this thesis a thorough analysis is presented on the effects of oxidation and oxide etching on the band structure of two dimensional silicon photonic crystals (2 D Si PC's). By using the plane wave expansion method (PWM), two structures of triangular lattice, namely, air cylinders embedded in a silicon background and silicon cylinders embedded in an air background are modeled. The thesis focuses on triangular lattice arrangement because for certain parameter values such a lattice can give rise to absolute band gap, which prohibits the propagation of either transverse electric (TE) or transverse magnetic (TM) polarizations.

During oxidation three processes occur simultaneously: silicon is consumed, consumed silicon is replaced by silicon dioxide, and silicon dioxide dimensions exceed the original silicon dimensions thereby displacing air. Each of these processes affects the photonic band gap differently. The first process causes the band gap to broaden and the latter two cause it to narrow. The contribution of each component to the overall change in the band gap is studied. In both structures the band gap is broadened and shifted up towards higher frequencies as the oxide grows. However, this is not a linear process; in each structure there is an oxide thickness value that gives rise to maximum change in band gap. This phenomenon is explained in terms of contribution from each component of the oxidation process.

The effect of oxide etching on the band structure is also studied. When the oxide is etched, the effective dielectric constant will decrease thereby broadening the band gap. The gap map variation follows different paths for oxidation and etching processes and the final positions are different. Thus, the band gap engineering can be performed by oxidation and/or etching.

For air cylinders embedded in a silicon background, it is demonstrated that a heterogeneous photonic crystal with enlarged band gap can be produced by localized oxidation. It is also demonstrated that localized oxidation in such a structure can result in a large cavity for band edge laser application. For silicon cylinders embedded in an air background, it is shown that a single defect cavity can be introduced by oxidizing the center cylinder. The defect frequency can be tuned by varying the oxide thickness.

Oxidation and etching are well controlled complementary metal oxide semiconductor (CMOS) compatible processing technologies. Our results clearly indicate that band gap engineering can be performed on Si PC's by these two processes.

I dedicate this work to my mother, Daw Yin Yin Nwe.

ACKNOWLEDGMENTS

First and foremost, I would like to thank my advisor, Dr. Sacharia Albin, for his guidance and support. I have been fortunate to benefit from his wisdom and insight. I would also express my gratitude to Dr. Helmut Baumgart and Dr. K. Vijayan Asari, two inspirational researchers, for agreeing to be on my thesis advisory committee despite their extremely busy schedules.

I would like to acknowledge Dr. Amin Dharamsi, Dr. Ei Ei Brown, Dr. Feng Wu and Dr. Shanping Guo for particularly helpful discussions in achieving the goal of this research. I heartily thank my colleagues and my friends: Pat Boland, Kurt Peters, Mike Mcvey, Ekrem, Ashu, Ming, Roopa and Heber, who I have learned from and enjoyed working with.

I dedicate my work to my loving family, my grand parents Sein, Thwai, Maung, Toke, and Than; my parents Yin Yin New, Khin Maung Maung and Vickie Chiodo-Maung; my siblings Su, Emily, Shela and Alex; and my cousins Thet, Eugene, Adrian and Tara.

Last but not least, my special mention goes to Thien whose support and understanding has made this research possible.

TABLE OF CONTENTS

LIST OF TABLES

Table Page

LIST OF FIGURES

CHAPTER I

INTRODUCTION

1.1 Motivation and Scope of Research

Ever since their architectural proposal by Yablonovich [1] in 1987, the photonic crystals (PC's) have fascinated the photonic physics and optoelectronic society as they offer control over the propagation of light in material medium. Recent upsurge in optical integration calls for devices that can allow or prohibit the propagation of certain frequencies in certain directions, enhance or suppress the rate of spontaneous emission, localize a light mode inside a cavity, and bend light with almost no loss. Since photonic band gap (PBG) materials allow for the engineering of devices with such features, increasing research has been devoted to them [2-12].

This thesis is primarily concerned with two dimensional photonic crystals, in which the dielectric function is periodic in two directions. An example of a 2-D PC is shown in Fig. 1.1. Two dimensional photonic crystals have drawn considerable attention over the past years due to their simple simulation, modeling and fabrication.

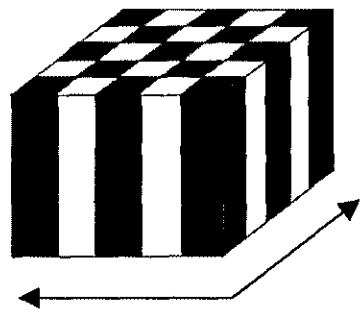

Fig.1.1.An example of a two dimensional photonic crystal, which is periodic in two directions. The diagram was taken from [35].

The use of 2-D PC's as wave guides, optical insulators and resonant cavities promises great potential for optical integration. When it comes to miniaturization, conventional methods used to guide light in the field of optical communication can be problematic. For example, in the case of index guiding in a doped/un-doped silica system, curvature bends may require several centimeters to accomplish a single optical function [13]; an example is shown in Fig. 1.2.

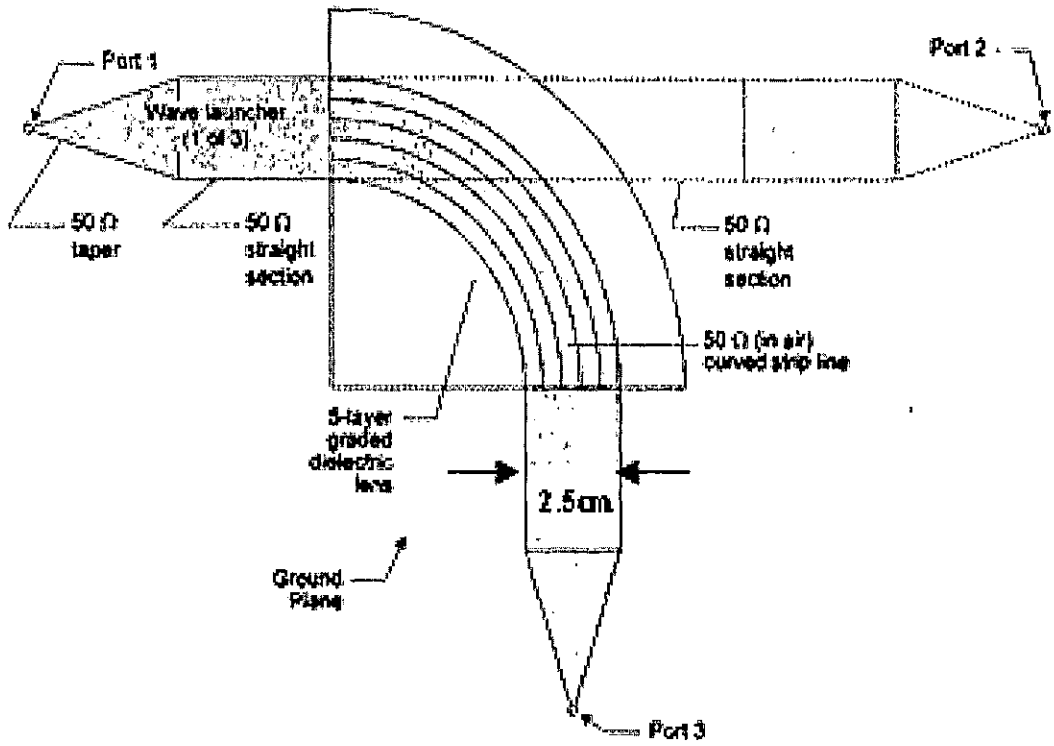

Fig. 1.2 A conventional wave guide bend system on centimeter scale. The diagram was taken from [13]

In two dimensional photonic crystals, light waves can be guided through a line defect which can bend at wavelength scale [14-18]; an example is shown in Fig. 1.3. In addition to such a line-defect-based wave guiding in photonic crystal slab, another type of wave

guiding, namely, coupled cavity guiding [19] can also be achieved in two dimensional photonic crystals. In such a wave guide, the neighboring defects are weakly coupled with each other so that light of a certain frequency range propagates by repeating power transition from one defect to another. As a result, light is transmitted with high efficiency through any sharp bend. Other important applications of two dimensional photonic crystals include, but are not limited to, optical fibers, point defect lasers, band-edge lasers, wavelength filters and polarizers [20-24].

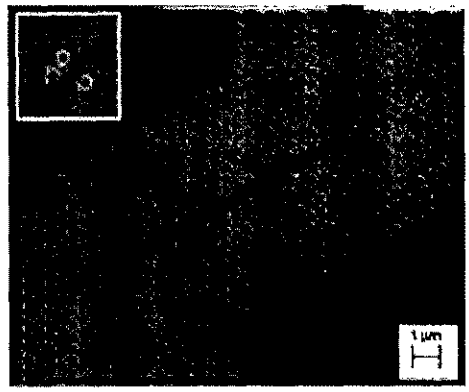

Fig. 1.3 A Line-defect-based photonic crystal wave guide on the micron scale. The diagram was taken from [14].

Utilizing silicon-based photonic crystal devices in optical circuits offers a variety of advantages because silicon-based photonic devices are process compatible with standard integrated circuit fabrication methods for devices such as CMOS. Mature, well-controlled silicon processing technology has made silicon an inherently advantageous optical material. Silicon especially finds its place in photonic band gap structures, since the high dielectric constant of silicon enables silicon photonic crystals to exhibit broad band gaps. Moreover, silicon is transparent to optical communication wavelengths 1.3~1.5μm;

therefore, infrared signals can propagate through the material without significant absorption loss. Hence, silicon photonic crystals have been a popular topic of research in the past decade [25-27].

Even though most photonic crystal fabrication challenges have been overcome, band gap engineering still remains relatively unexplored. To accommodate ever increasingly complex design and functionality for photonic devices, tailoring and manipulating the photonic band gap is required. In this thesis, the effects of thermal oxidation and oxide etching, two fundamental processes in silicon technology, on the band gap of silicon photonic crystals is studied.

By using the plane wave expansion method [28], we modeled (i) a two dimensional silicon photonic crystal consisting of air cylinders embedded in a silicon background and (ii) a two dimensional silicon photonic crystal consisting of silicon cylinders in an air background. See Fig. 1.4 (a) and (b). This thesis presents an analysis of the evolution of the photonic band structure during the oxidation and oxide etching processes on both structures.

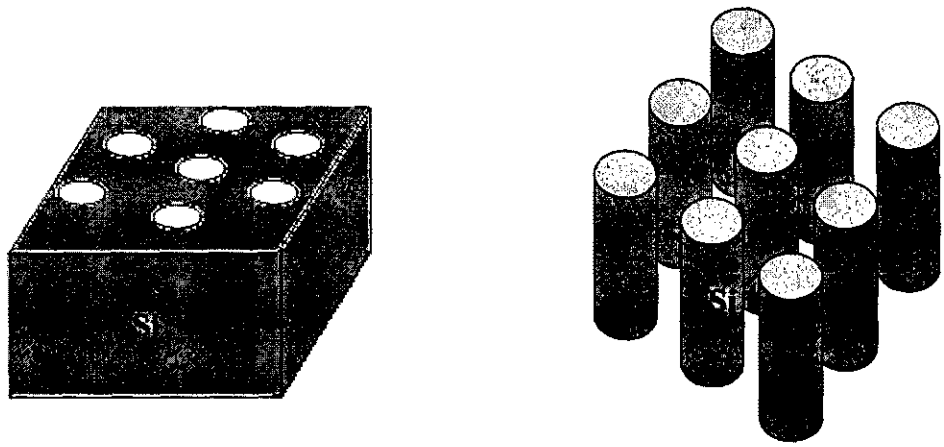

(a) (b)

Fig. 1.4 (a) 2-D PC consisting of air cylinders in Si background (b) 2-D PC consisting of Si cylinders in air background.

Based on the results, a few possible applications for the Si/SiO_2/air PC structures are discussed. Methods to fine tune the band gap on Si PCs are presented. In the first example, band gap enlargement in a heterogeneous photonic crystal formed by localized oxidation is analyzed. In the second example, light confinement in a large cavity formed by selective oxidation is also proposed. This result is useful for band edge laser application. In the third example, a single defect cavity is introduced by oxidizing the center cylinder, and defect frequency tuning is demonstrated by varying the oxide thickness. Oxidation and etching are highly controllable CMOS processes that are suitable for integration of high-speed silicon modulators [29] and Raman lasers [30,31]; the results will illustrate the effects of these two processes on Si PC's.

1.2 Literature Review

[32, 33] and [14] are some of the few studies done on the oxidation of Si PC's. [14] mentions as a side point that the band gap shifts upward as the oxide grows. No analysis is presented. [32] models the band gap of air cylinder structure during oxidation, in which the oxide grows only inside silicon and the air hole radius remains unchanged. The effect of silicon dioxide expansion due to the volume ratio of consumed Si to grown SiO_2 is disregarded. [33] models both air cylinder and Si cylinder structures but the non-linear nature of band gap change due to oxidation is not discussed. In this thesis, certain subtleties of the dynamics on the oxidation process that have been overlooked in previous studies are included.

1.3 Photonic Band Gap: Theoretical Background

Complete control over light propagation has become extremely valuable for a wide range of applications in optical engineering. An interesting analogy lies between semiconductor electronic materials and photonic crystal materials. The principles of photonic band gap are explained in this chapter. The similarities between lattice structures for successful control of electron propagation in electronic materials and photon propagation in photonic materials will be evident.

1.3.1 Formation of Energy Band Gap for Electron Propagating in Semiconductor Lattice

The periodic structure of semiconductor materials gives rise to the periodic potential to the propagating electrons. Hence, the geometry of the crystal governs the flow of electrons. In Fig. 1.5, the energy versus wave vector ($\vec{k}$) diagrams for an electron traveling through a vacuum and a periodic medium such as a semiconductor are compared.. In Fig. 1.5 (a) the energy curve is smooth. However, for an electron propagating through a material with periodic electric potential, the energy is discontinuous at Bragg reflection points as shown in Fig. 1.5 (b).

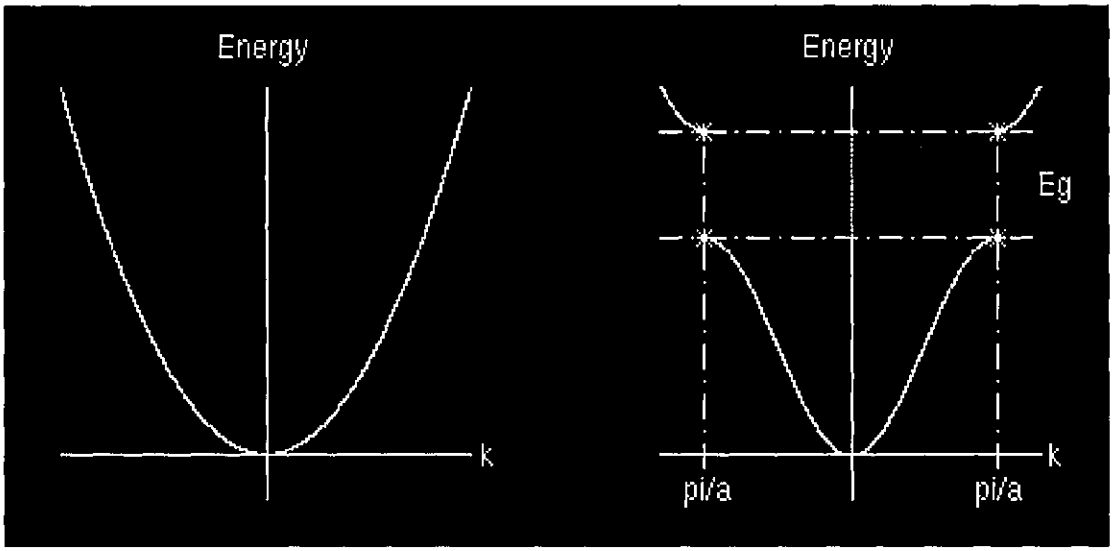

Figure 1.5. (a) Energy versus wave vector for an electron in vacuum
(b) Energy band gap formed for an electron in a periodic medium with lattice constant a. The diagram is taken from [34].

As de Broglie suggested, a wave function can be assigned to a propagating electron. The probability of finding an electron at a certain location can be determined by the Schrodinger equation. However, Bragg reflection occurs at the locations where the following Bragg condition is met.

$$\vec{k} = \pm\frac{n\pi}{a} \tag{1.1}$$

where $\vec{k}$ is the wave vector, n is an integer and a is the lattice constant.

Bragg reflections can disturb the wave function of the electron and at the locations where the Bragg condition is met, the wavelike solution to the Schrodinger equation of the electron does not exist. As a result, a gap is formed between two energy curves, and electrons with energies that lie within the gap cannot propagate at these wave vector values. This gap is called the energy band gap or the forbidden band of the semiconductor.

1.3.2 Photonic Band Gap in Macroscopic periodic structures

The same concept is developed in photonic crystals based on the macroscopic periodic structure of the dielectric materials. In an attempt to imitate the periodic structure of electronic materials, photonic band gap materials are formed by arranging the materials of high dielectric constants in periodic arrays. Therefore, the electromagnetic wave propagating through such a medium will experience a periodic dielectric function giving rise to a forbidden gap for photons.

1.3.3 One dimensional, two dimensional and three dimensional photonic crystals

One dimensional photonic crystals, commonly known as dielectric multi-layers are relatively easy to understand and the same ideology can be applied to two and three dimensional cases. In the one-dimensional case, as shown in Fig. 1.6 (a) layers of two different dielectric materials alternate along one direction periodically. Because of this periodic spatial arrangement, the dielectric constant becomes position dependent, and it is commonly known as the dielectric function. Due to the periodic arrangement of the layers, certain frequencies of light propagating in the direction perpendicular to the interface of the dielectric layers are forbidden. As a result, allowed bands and forbidden bands are formed. In a two dimensional case, the dielectric function is periodic in two directions as shown in Fig. 1.6 (b). In a three dimensional case, where the layers alternate periodically in three directions as shown in Fig. 1.6 (c), light with certain frequencies is forbidden from propagating regardless of the direction. Such a band gap is called a complete photonic band gap. In the case of semiconductor materials, when impurities are

introduced, allowed energies appear within the energy band gap. In a perfect analogy, when disorder or defects are introduced in the periodic dielectric structure, we can create the light modes in the middle of the band gap, which are highly localized around the defect.

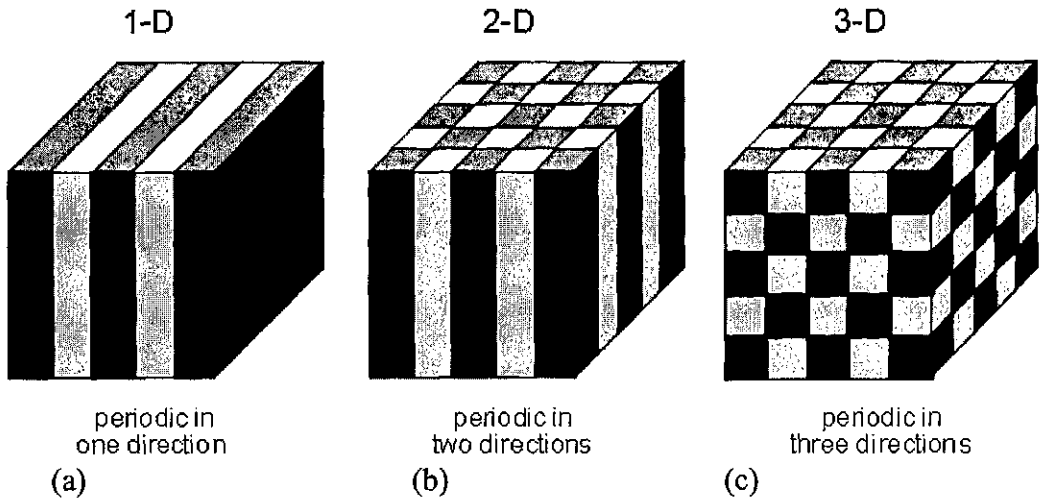

Fig. 1.6 (a) One dimensional PC (b) two dimensional PC (c) three dimensional PC. The diagram is taken from [35].

1.3.4 Eigenvalue Problem

A common theoretical approach to photonic crystals is rearranging Maxwell's equations to constitute an eigenvalue problem for harmonic Fourier components of electric and magnetic fields. When four Maxwell's equations are rearranged by means of elementary calculus the following Helmholtz equation is obtained.

$$\nabla \times \frac{1}{\varepsilon(r)} \nabla \times \overline{H} = \frac{\omega^2}{c^2} \mu . \overline{H} \tag{1.2}$$

The operator on the left hand side of the eigenvalue equation, (1.2), is a positive definite Hermitian operator that has positive real eigenvalues. From these eigenvalues we can

calculate the corresponding frequencies. On the other hand, the periodic dielectric function $\frac{1}{\varepsilon(r)} = u_{\vec{k}}(r)$ can be expressed in a Fourier series by summing over reciprocal lattice vector, $\vec{G}$. In addition, according to Bloch's theorem, the electric field or magnetic field in the periodic medium is the product of the periodic potential function and the plane wave. Therefore, the electromagnetic (EM) fields take the form

$$\overline{H} = u_{\vec{k}}(r) \cdot e^{j\vec{k}.\vec{r}} = \sum_{\vec{G}} h(\vec{G}) \cdot e^{j\vec{G}.\vec{r}} \cdot e^{j\vec{k}.\vec{r}} = \sum_{\vec{G}} h(\vec{G}) \cdot e^{j(\vec{k}+\vec{G}).\vec{r}} \tag{1.3}$$

where $u_{\vec{k}}(r)$ is the periodic dielectric potential and $h(\vec{G})$ is its Fourier coefficient. From the eigenvalue equation (1.2) it can be seen that only the eigen frequencies can propagate. Therefore, allowed and forbidden frequency bands are formed. Hermicity of the operator also requires that all the eigen modes are orthogonal to each other. A detailed explanation is presented in Chapter III and further mathematical details are presented in Appendix I.

1.3.5 Analogy with Schrodinger's wave equation for electrons

It can also be said that the eigenvalue equation of $\overline{H}$, equation (1.2), is analogous to the following Schrodinger's wave equation for electrons.

$$[-\frac{\hbar}{2m}\nabla^2 + V(r)]\psi(r,t) = i\hbar\frac{\partial\psi(r,t)}{\partial t} \tag{1.4}$$

where $V(r) = V(r+R)$ is the periodic potential function and the wave function $\psi(r,t)$ is the sum of waves.

$$\psi(r,t) = \sum_{l=1}^{\infty}\sum_{m=1}^{\infty} a_{lm} e^{i(k_l x - \omega_m t)} \tag{1.5}$$

As can be seen in both cases, the wave function is decomposed into its harmonic components and the eigen modes are determined by the Hermitian eigenvalue equation.

The other important analogy is that the symmetry properties of the quantum-mechanical potential function V and that of the dielectric function $u_{\vec{k}}$ largely simplify the problem. One advantage of the optical problem is that photons, unlike electrons, have no fundamental length scale such as Bohr's radius. In the case of an electron propagating in semiconductor lattice, configurations that differ only by their absolute length scale have very different properties because the potential function has the fundamental length scale of Bhor's radius. However, in an electromagnetic problem, when all the distances are contracted or expanded by a factor, the eigenvalue (or) frequency is scaled by the same factor. Therefore, the results of the calculations in one length scale can be extrapolated to obtain the solutions of the problem at other scales.

CHAPTER II

THEORY: NUMERICAL CALCULATIONS BY PLANE WAVE EXPANSION METHOD

There are several numerical techniques that are capable of determining how light will propagate through a particular periodic structure (eg. FDTD method, FDFD method) [36,37]. The modeling method used in this thesis is called the plane wave expansion method (PWM)[28]. It is one of the most studied methods, since it can provide reliable results even though the accuracy is commensurate with computing time.

2.1 Mathematical Details of Plane Wave Expansion Method

(a) Fourier series representation of the periodic dielectric function

In photonic crystals, the electromagnetic (EM) waves propagate through a periodic medium. Therefore parameters such as ε and μ are periodic functions which have the same period as the medium. Let us suppose $u_{\vec{k}}(r)$ is such a periodic function. Like any other periodic functions, $u_{\vec{k}}(r)$ can be expanded into Fourier series. It can be represented as the sum over various wave vectors.

$$u_{\vec{k}}(r) = \sum_{\vec{k}} \zeta(\vec{k}).e^{j\vec{k}.\vec{r}} \qquad \text{where } \vec{k} \text{ is the wave vector} \tag{2.1}$$

However, since $u_{\vec{k}}(r)$ is a periodic function, $u_{\vec{k}}(r) = u_{\vec{k}}(r+R)$, where R is the period of the function,

$$u_{\vec{k}} = \sum_{\vec{k}} \zeta(\vec{k}).e^{j\vec{k}.\vec{r}} = \sum_{\vec{k}} \zeta(\vec{k}).e^{j\vec{k}.(\vec{r}+\vec{R})} = \sum_{\vec{k}} \zeta(\vec{k}).e^{j\vec{k}.\vec{r}}.e^{j\vec{k}.\vec{R}} \tag{2.2}$$

In order for (2.2) to be satisfied, $e^{j\vec{k}.\vec{R}}$ must be equal to 1 or the coefficient for that k value, $\zeta(\vec{k})$, must be zero. In other words, $\zeta(\vec{k})$ will be zero, unless $\vec{k}.\vec{R} = 2n\pi$. Therefore, in the Fourier series, only the coefficients, $\zeta(\vec{k})$, whose $\vec{k}$ value satisfies the condition $\vec{k}.\vec{R} = 2n\pi$ survive and the rest are zero. Such wave vectors are called reciprocal lattice vectors and denoted by $\vec{G}$. Hence, it is sufficient if we sum up the $\vec{G}$ vectors instead of all $\vec{k}$.

$$u_{\vec{k}}(r) = \sum_{\vec{G}} \zeta(\vec{G}).e^{j\vec{G}.\vec{r}} \tag{2.3}$$

$\varepsilon(r)$ and $\mu(r)$ are expanded into such series as shown below. For convenience, instead of $\varepsilon(r)$, $\frac{1}{\varepsilon(r)}$ will be expanded into the Fourier series, since the $\frac{1}{\varepsilon(r)}$ term appears in the Helmholtz equation that needs to be solved.

$$\frac{1}{\varepsilon(r)} = \sum_{\vec{G}} u_{\vec{k}}(\vec{G}).e^{j\vec{G}.\vec{r}} \tag{2.4}$$

$$\mu(r) = \sum_{\vec{G}} \eta(\vec{G}).e^{j\vec{G}.\vec{r}} \tag{2.5}$$

(b) Bloch's Theorem and series representation of H field

Bloch's theorem states that a Bloch mode in a periodic medium is the product of the periodic function and a plane wave. Therefore, $\overline{H}$ can be represented as

$$\overline{H} = u_k \cdot e^{j\vec{k}.\vec{r}} = \sum_{\vec{G}} h(\vec{G}).e^{j\vec{G}.\vec{r}}.e^{j\vec{k}.\vec{r}} = \sum_{\vec{G}} h(\vec{G}).e^{j(\vec{k}+\vec{G}).\vec{r}} \tag{2.6}$$

where $h(G)$ is the Fourier coefficient of the $\overline{H}$ field. According to (2.6), the wave is propagating in the $\vec{k}+\vec{G}$ direction. Therefore, the direction of the $\overline{H}$ field needs to be perpendicular to $\vec{k}+\vec{G}$. Now we will define a set of orthogonal unit vectors $\overline{e}^{\lambda}$, λ=1,2 where $\overline{e}^{1}$, $\overline{e}^{2}$ and $\vec{k}+\vec{G}$ are mutually perpendicular. Therefore, $\overline{H}$ will have two components $\overline{e}^{1}$, $\overline{e}^{2}$ and each of the coefficients $h(\vec{G})$ can be decomposed into these two components; (2.6) becomes,

$$\overline{H} = \sum_{\vec{G}} \sum_{\lambda} \overline{e}^{\lambda} h(\vec{G})\, e^{j(\vec{k}+\vec{G}).\vec{r}} \tag{2.7}$$

(c) Transforming Helmholtz equation into matrix form

The following is the Helmholtz equation or the wave equation, which is the result of the Maxwell equations.

$$\nabla \times \frac{1}{\varepsilon(r)} \nabla \times \overline{H} = \frac{\omega^2}{c^2} \mu . \overline{H} \tag{2.8}$$

By substituting (2.4), (2.5) and (2.7) into (2.8), the Helmholtz equation (2.8) can be transformed into algebraic form as in (2.9). Mathematical details of the derivation are presented in Appendix I.

$$\sum_{\vec{G}'} \left|\vec{k}+\vec{G}'\right|\left|\vec{k}+\vec{G}\right| \varepsilon^{-1}(\vec{G}-\vec{G}') \begin{pmatrix} \vec{e}^{2} \bullet \vec{e}^{2'} & -\vec{e}^{2} \bullet \vec{e}^{1'} \\ -\vec{e}^{1} \bullet \vec{e}^{2'} & \vec{e}^{1} \bullet \vec{e}^{1'} \end{pmatrix} \begin{pmatrix} h_1' \\ h_2' \end{pmatrix} = \frac{\omega^2}{c^2} \begin{pmatrix} h_1 \\ h_2 \end{pmatrix} \tag{2.9}$$

where $\overline{e}^{1}, \overline{e}^{2}$ are two orthogonal vectors each of which is also orthogonal to $\vec{k}+\vec{G}$; h_1 is the component of $\overline{H}$ in the x-y plane and h_2 is the component in z direction. It can be

seen that (2.9) constitutes a standard eigenvalue problem which can be written in matrix form as in (2.10).

$$\begin{pmatrix} M_1 & M_2 \\ M_3 & M_4 \end{pmatrix} \begin{pmatrix} h_1(G') \\ h_2(G') \end{pmatrix} = \frac{\omega^2}{c^2} \begin{pmatrix} h_1(G) \\ h_2(G) \end{pmatrix} \tag{2.10}$$

Therefore, the eigen frequencies can be obtained by standard diagonalization of the matrix in (2.10). Moreover, in a two dimensional case, where the $\vec{k}$ vector is confined in the x-y plane, $\bar{e}^{2}, \bar{e}^{2'}$ are in the z direction and $\bar{e}^{1}, \bar{e}^{1'}$ are in the x-y plane. Therefore, the matrix form is reduced to (2.11).

$$\begin{pmatrix} M_1 & 0 \\ 0 & M_4 \end{pmatrix} \begin{pmatrix} h_1(G') \\ h_2(G') \end{pmatrix} = \frac{\omega^2}{c^2} \begin{pmatrix} h_1(G) \\ h_2(G) \end{pmatrix} \tag{2.11}$$

Hence, the two polarizations h_1 and h_2 can be decoupled to give rise to transverse magnetic (TM) modes and transverse electric (TE) modes as in (2.12) and (2.13).

TM:
$$\sum_{G'} \left|\vec{k} + \vec{G}'\right| \left|\vec{k} + \vec{G}\right| \varepsilon^{-1}(\vec{G} - \vec{G}') h_1(G') = \frac{\omega^2}{c^2} h_1(G) \tag{2.12}$$

TE:
$$\sum_{G'} \left(\vec{k} + \vec{G}'\right) \bullet \left(\vec{k} + \vec{G}\right) \varepsilon^{-1}(G - G') h_2(G') = \frac{\omega^2}{c^2} h_2(G) \tag{2.13}$$

2.2 Applying the PWM method to the two dimensional PC of triangular lattice

(a) PC of triangular lattice

In this thesis two dimensional photonic crystals with (i) air cylinders embedded in a silicon background and (ii) silicon cylinders embedded in an air background are studied.

The embedded cylinders are often referred to as atoms. The specific arrangement of the atoms shown in Fig. 2.1 (a) is called the triangular lattice structure. Among different lattice arrangements triangular lattice attracts more attention than others because for certain radius parameters and filling ratios it provides an absolute band gap which prohibits propagation of certain frequencies for either TE or TM polarization. Therefore, in this thesis the photonic band structure of PC with a two dimensional triangular lattice is studied. In such a lattice, the PC can be divided into elementary unit cells each containing one atom as shown in Fig. 2.1 (b).

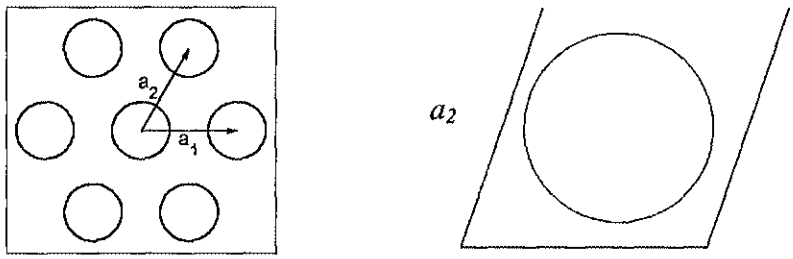

(a) (b)

Fig. 2.1 (a) Cylinders embedded in the background material in triangular lattice arrangement (b) a unit cell of triangular lattice containing one atom.

(b) Relation between lattice vectors and reciprocal lattice vectors of a triangular lattice

As described in section 2.1, and according to Bloch's theorem, to obtain series representation of EM fields it is sufficient to sum over reciprocal vectors $\vec{G}$ rather than all the wave vector $\vec{k}$. Therefore, our study is reduced to the first Brillouin zone in spectral domain. This first Brillouin zone is highlighted in Fig. 2.2. (b). Due to the symmetry of the structure, it can be seen that we can reduce our study further to the irreducible Brillouin zone that is represented by the darkened region in Fig. 2.2 (b). The relation between direct lattice vectors $\vec{a}_1, \vec{a}_2$ and the components of reciprocal lattice

vector $\vec{G}$: $\vec{b}_1$ and $\vec{b}_2$ in Fig. 2. 2 (b) are tabulated in Table 1. The ratio of the cross sectional area of the atom to the area of the unit cell is often referred to as filling ratio *f*, and it turns out to be a critical parameter in determining the photonic band structure.

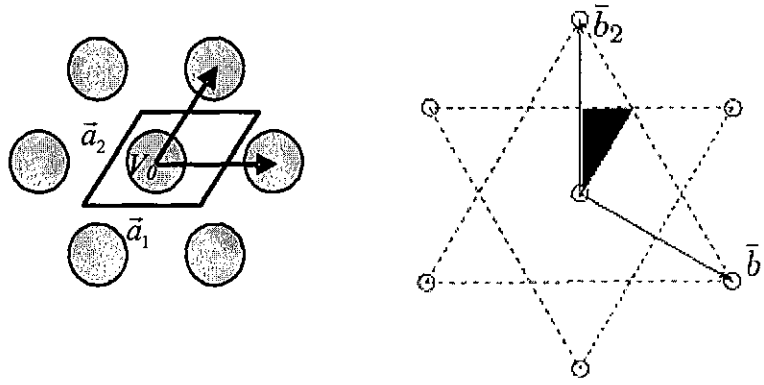

(a) (b)

Fig.2.2 (a) Direct lattice vectors in real space domain (b) reciprocal lattice vectors in spectral domain. The first Brillouin zone is highlighted and the irreducible Brillouin zone is the darkened region.

Table 2.1. Relation between direct lattice vectors and reciprocal lattice vectors

Direct lattice vectors	
$\vec{a}_1$	$a(1,0)$
$\vec{a}_2$	$a(1/2,\sqrt{3}/2)$
Reciprocal lattice vectors	
$\vec{b}_1$	$2\pi/a(1,-\sqrt{3}/3)$
$\vec{b}_2$	$2\pi/a(0,2\sqrt{3}/3)$
Area of the unit cell: V_0	$\lvert\vec{a}_1\times\vec{a}_2\rvert=\sqrt{3}a^2/2$
Filling ratio: f	$\pi R^2/(\sqrt{3}a^2/2)$ (R is the radius of the atom)

2.3 Mathematical Derivation of the Fourier Coefficient of the Air/SiO_2/Si Structure

So far, we have constructed an eigenvalue system for $\vec{H}$. To solve for the eigen frequencies in (2.12) and (2.13) in section 2.1, it is necessary to evaluate the Fourier coefficients of the dielectric function, $\frac{1}{\varepsilon(r)}$. The derivation of this coefficient varies with the geometry of the structure being modeled. Since our specific structure of interest consists of three different dielectric materials, namely, air, SiO_2 and Si, in this section the derivation of the Fourier coefficient will be presented for 2-D PC of $\varepsilon_a / \varepsilon_b / \varepsilon_c$. The unit cell of the structure is shown in Fig. 2.3.

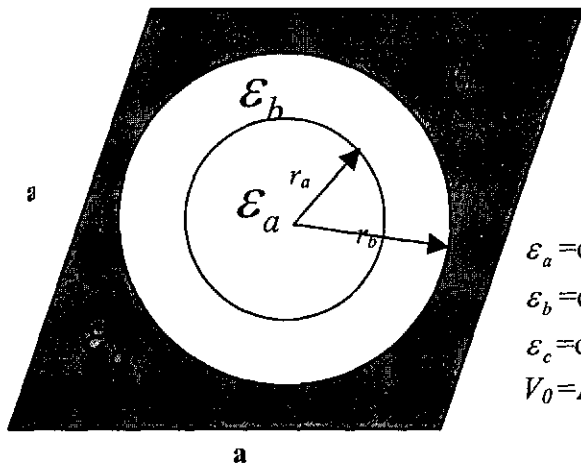

ε_a =dielectric constant (medium a)
ε_b =dielectric constant (medium b)
ε_c =dielectric constant (medium c)
V_0 =Area of the unit cell

Fig. 2.3 A unit cell of 2-D triangular PC consisting of three dielectric materials.

Recalling the Fourier shift property,

if $\mathbf{F}\{K(r)\} = K(G)$,

$\mathbf{F}\{K(r+R)\} = e^{jGR} K(G)$.

Therefore, if Fourier transform of a unit cell is known, we can use the Fourier shift property to obtain the Fourier transform of a collection of unit cells (supercell) by addition.

$$\mathbf{F}\{\sum_{R_i} K(r+R_i)\} = \sum_{R_i} e^{jG.R_i} K(G)$$

The dielectric function of the structure in one unit cell shown in Fig. 2.3 can be written as,

$$\frac{1}{\varepsilon(r)} = K(r) = \frac{1}{\varepsilon_c} + \left(\frac{1}{\varepsilon_a} - \frac{1}{\varepsilon_c}\right) S \tag{2.14}$$

where:

$$S = \begin{cases} 1 & r \le r_a \\ \dfrac{\varepsilon_a \varepsilon_c}{\varepsilon_c - \varepsilon_a}\left(\dfrac{1}{\varepsilon_b} - \dfrac{1}{\varepsilon_c}\right) & r_a < r \le r_b \\ 0 & r > r_b \end{cases}$$

$$K(\bar{G}) = \frac{1}{Vo}\int_{Vo} \frac{1}{\varepsilon(r)} d\bar{r}[e^{-j\bar{G}\bullet\bar{r}}]$$

$$= \frac{1}{Vo}\int_{Vo}\left[\frac{1}{\varepsilon_c} + \left(\frac{1}{\varepsilon_a} - \frac{1}{\varepsilon_c}\right) S\right] e^{-j\bar{G}\bullet\bar{r}} d\bar{r}$$

$$K(\bar{G}) = \frac{1}{Vo}\int_{Vo} \frac{1}{\varepsilon_c} e^{-j\bar{G}\bullet\bar{r}} d\bar{r} + \frac{1}{Vo}\int_{Vo}\left(\frac{1}{\varepsilon_a} - \frac{1}{\varepsilon_c}\right) S e^{-j\bar{G}\bullet\bar{r}} dr$$

$$= \frac{1}{\varepsilon_c}\delta(\bar{G}) + \frac{1}{Vo}\int_0^{r_a}\int_0^{2\pi}\left(\frac{1}{\varepsilon_a} - \frac{1}{\varepsilon_c}\right)\cdot 1 e^{-j\bar{G}\bullet\bar{r}} r d\theta dr$$

$$+ \frac{1}{Vo}\int_{r_a}^{r_b}\int_0^{2\pi}\left(\frac{1}{\varepsilon_a} - \frac{1}{\varepsilon_c}\right)\frac{\varepsilon_a \varepsilon_c}{\varepsilon_c - \varepsilon_a}\left(\frac{1}{\varepsilon_b} - \frac{1}{\varepsilon_c}\right)\cdot 1 e^{-j\bar{G}\bullet\bar{r}} r d\theta dr$$

$$= \frac{1}{\varepsilon_c}\sigma(\overline{G}) + \frac{1}{V_0}\left(\frac{1}{\varepsilon_a} - \frac{1}{\varepsilon_c}\right)\underbrace{\int_0^{r_a}\int_0^{2\pi} e^{-jGr\cos\theta} r\,d\theta dr}_{I_1}$$

$$+ \frac{1}{V_0}\left(\frac{1}{\varepsilon_b} - \frac{1}{\varepsilon_c}\right)\underbrace{\int_{r_a}^{r_b}\int_0^{2\pi} e^{-jGr\cos\theta} r\,d\theta dr}_{I_2} \tag{2.15}$$

$$I_1 = \int_{r_a}^{r_b}\int_0^{2\pi} e^{-jGr\cos\theta} r\,d\theta dr$$

$$= \int_{r_a}^{r_b}\int_0^{2\pi} e^{jGr\sin(\theta-\frac{\pi}{2})} r\,d\theta dr \tag{2.16}$$

Using Bessel series expansion

$$e^{jw\sin\phi} = \sum_{l=-\infty}^{\infty} J_l(w) e^{jl\phi}$$

$$e^{jGr\sin(\theta-\frac{\pi}{2})} = \sum_{l=-\infty}^{\infty} J_l(Gr) e^{jl(\theta-\frac{\pi}{2})} \tag{2.17}$$

From (2.16) and (2.17)

$$I_1 = \int_{r_a}^{r_b}\int_0^{2\pi}\sum_{l=-\infty}^{\infty} J_l(Gr) e^{jl(\theta-\frac{\pi}{2})} r\,d\theta dr$$

$$= \int_{r_a}^{r_b}\int_{0}^{2\pi} rJ_o(Gr)d\theta dr \qquad \text{(Only } J_o \text{ term survives.)}$$

$$= \int_{r_a}^{r_b} 2\pi r J_o(Gr)dr$$

$$= 2\pi \int_{r_a}^{r_b} rJ_o(Gr)dr = 2\pi \int_{r_a}^{Gr_a} \frac{x}{G^2} J_o(x)dx \qquad (2.18)$$

Using the property $d[wJ_1(w)] = wJ_0(w)$

$$wJ_1(w) = \int wJ_0(w)\,dw$$

$$I_1 = \frac{2\pi}{G^2}\left[xJ_1(x)\right]_0^{Gr_a} = \frac{2\pi}{G} r_a J_1(Gr_a) \qquad (2.19)$$

Similarly,

$$I_2 = \frac{2\pi}{G^2}\left[xJ_1(x)\right]_{Gr_a}^{Gr_b} = \frac{2\pi}{G}\left[r_b J_1(Gr_b) - r_a J_1(Gr_a)\right] \qquad (2.20)$$

By substituting (2.19) and (2.20) in (2.15), we can obtain the Fourier coefficient for our structure in (2.21a) and (2.21b).

For $G \neq 0$,

$$K(\vec{G}) = \frac{1}{\varepsilon_c}\delta(G) + \frac{2\pi}{GV_0} r_a J_1(Gr_a)\left(\frac{1}{\varepsilon_a} - \frac{1}{\varepsilon_c}\right) + \frac{2\pi}{GV_0}\left(\frac{1}{\varepsilon_b} - \frac{1}{\varepsilon_c}\right)\left[r_b J_1(Gr_b) - r_a J_1(Gr_a)\right] \qquad (2.21a)$$

For $G = 0$,

$$K(G) = \frac{1}{\varepsilon_c} + \frac{\pi r_a^{\,2}}{V_0}\left(\frac{1}{\varepsilon_a} - \frac{1}{\varepsilon_c}\right) + \frac{\pi(r_b^{\,2} - r_a^{\,2})}{V_0}\left(\frac{1}{\varepsilon_b} - \frac{1}{\varepsilon_c}\right) \qquad (2.21b)$$

2.4 Algorithm Implementation

The algorithm is implemented in MATLAB code since MATLAB is designed to work most efficiently with matrices. Our goal is to calculate the eigen frequencies of TE and TM modes from (2.12), (2.13) and to plot them against various $\vec{k}$ vectors generating dispersion curves. The following implementation procedure was performed to achieve our goal:

1. Construct reciprocal lattice vectors G's from the direct lattice vectors $\vec{a}_1, \vec{a}_2$.
2. Obtain the Fourier transform of the dielectric function $\varepsilon^{-1}(G)$. This is the Fourier transform of one unit cell. Use the Fourier shift property to obtain the Fourier transform of a supercell (a collection of unit cells).
3. Specify the number of plane waves to be used.
4. Form the matrix $\varepsilon^{-1}(G-G')$. Since it has two indices G and G', it is a square matrix of NxN ,where N is the number of plane waves used in the calculation.
5. Form an array of $\vec{k}$ vectors along the edges of the irreducible Brillouin zone.
6. Form the corresponding eigen matrix from (2.12), (2.13) for TE and TM modes.
7. Obtain eigen frequencies from MATLAB eigen solver.
8. Plot the normalized frequency a/λ against the wave vector $\vec{k}$ values along the edges of the irreducible Brillouin zone, thereby generating dispersion curves.

A diagram of typical dispersion curves and the photonic band gap is shown in Fig. 2.4. The x-axis is the $\vec{k}$ vector values along the edges of the irreducible Brillouin zone and the y-axis is normalized frequency a/λ. The dotted curves and the solid curves represent

the TE and TM modes respectively. The TM band gap is formed between the maximum of TM mode 1 and the minimum of TM mode 2. The TE band gap is found between TE mode 1 and 2. In some structures, where there is an overlap between TE and TM band gaps, an absolute band gap can be obtained. Such a band gap forbids propagation of either polarization.

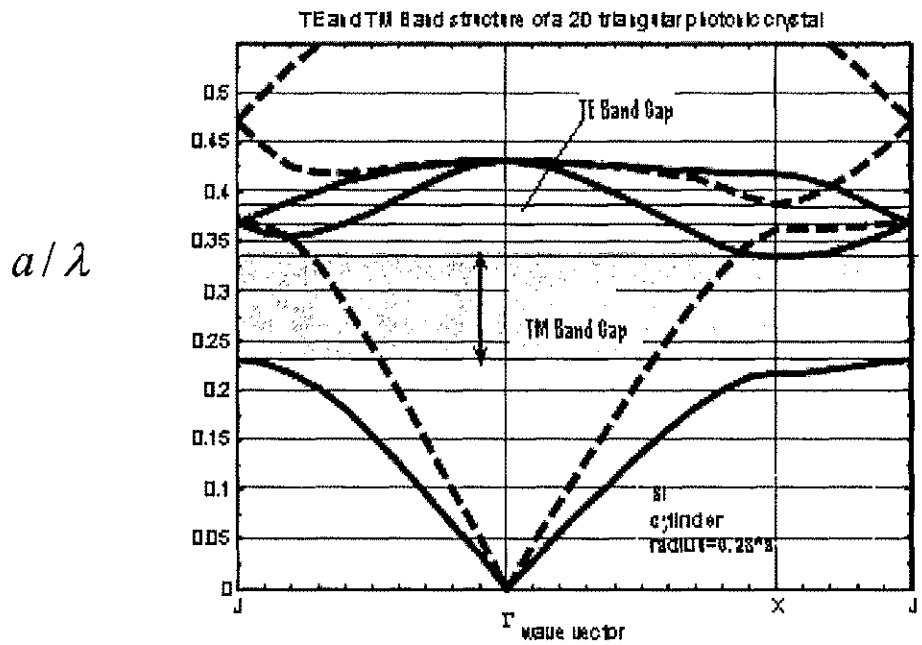

Fig. 2.4 A typical photonic band diagram.

CHAPTER III

EFFECT OF OXIDATION AND OXIDE ETCHING ON THE PHOTONIC BAND GAP : AIR CYLINDERS EMBEDDED IN SILICON

3.1 Calculation of the radius parameters during oxidation

A specific model of a 2-D silicon photonic crystal consisting of air holes that have a radius of $0.42a$ is chosen to demonstrate the dynamics of the radius parameters involved in the oxidation process, where a is the lattice constant. We have chosen the radius of $0.42a$ to ensure that the interface between silicon and silicon dioxide is contained within the unit cell after oxidation. The largest radius that can be contained in a triangular lattice unit cell is $0.433a$. The relation between oxide thickness t, and the radii of the air hole r_a and the oxide-silicon interface r_c is calculated as follows.

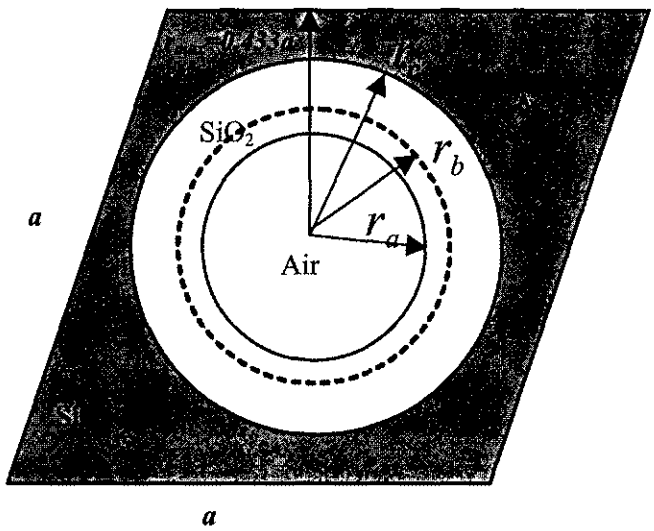

r_a: radius of the air hole after oxidation,
r_b: radius of the air hole before oxidation,
r_c: radius of the interface circle between the silicon and silica,
ε_a: permittivity of the air 1,
ε_b: permittivity of SiO_2 2.09,
ε_c: permittivity of silicon 12.08, and
A_0: the area of the unit cell.

Fig. 3.1. Oxidation of silicon around air hole in a single unit cell of triangular lattice.

In the simulation, we assumed an oxide growth process, where the ratio between the volume of silicon consumed and the volume of SiO_2 generated is equal to 0.44 [38]. The height of the cylinder is assumed to be infinite. Therefore,

$$\frac{\pi r_c^2 - \pi r_b^2}{\pi r_c^2 - \pi r_a^2} = \frac{r_c^2 - r_b^2}{r_c^2 - r_a^2} = 0.44 \tag{3.1}$$

By defining the thickness of the oxide layer t as

$$t = r_c - r_a \tag{3.2}$$

we obtain:

$$r_c = \sqrt{(0.44t)^2 - 0.44t^2 + r_b^2} + 0.44t = \sqrt{r_b^2 - 0.2464t^2} + 0.44t \tag{3.3}$$

$$r_a = \sqrt{(0.56t)^2 - 0.56t^2 + r_b^2} - 0.56t = \sqrt{r_b^2 - 0.2464t^2} - 0.56t \tag{3.4}$$

(3.3) and (3.4) constrain the original air hole radius and oxide thickness. In (3.3), the original air hole radius r_b and oxide thickness t must be chosen in such a way that r_c is less than $0.433a$. In other words, the silicon and silicon dioxide interface must be contained in the unit cell. In (3.4), the values of r_b and t must be chosen such that r_a is greater than zero. This will ensure that the air hole is not completely closed due to oxidation.

3.2 Results and Discussion

The dielectric constant of Si and SiO_2 were chosen as 12.08 and 2.09 respectively near the optical communication wavelength. The plane wave expansion method [28] was used to calculate the band structure. The number of plane waves in the Fourier expansion is 169. Increasing the number of plane waves does not seem to affect the results significantly.

Our model generates the dispersion curves for the structure with the parameter values of $r_a = 0.4069a$, $r_b = 0.42a$ and $r_c = 0.43a$ as shown in Fig. 3.2. Before oxidation, the original structure 1 has air holes of radius $r_b = 0.42a$ in the Si background. The upper and lower bands of the TM gap of structure 1 give rise to an absolute band gap in Fig. 3.2. Since the TM gap lies inside the TE band gap, this is an absolute band gap. The TE bands are not shown.

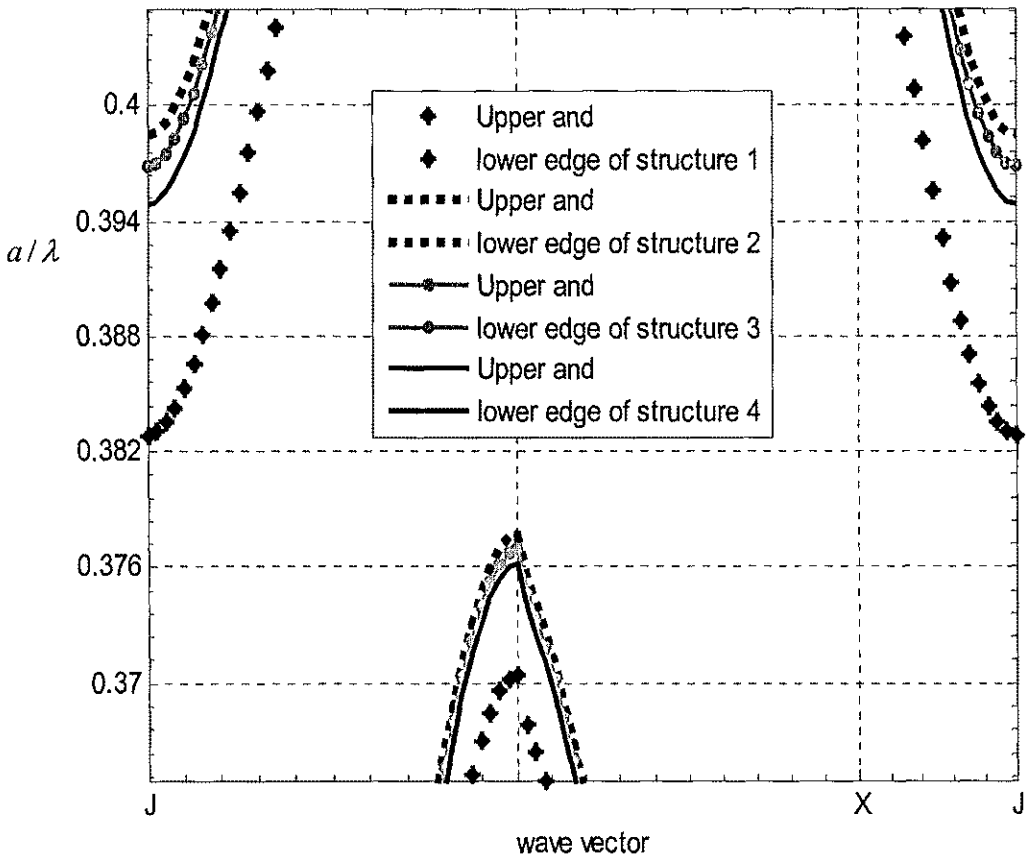

Fig. 3.2. The TM dispersion curves giving rise to the absolute band gap for the structure consisting of air holes in Si background. structure1 (starting point): when the air hole radius in the Si background is 0.42a, structure 2: when silicon is consumed and the air hole radius becomes 0.43a, structure 3: when consumed Si is replaced by SiO_2, structure 4: when the air hole shrinks due to SiO_2 volume expansion.

The structure is oxidized until the radius of the Si/SiO_2 interface, r_c, becomes $0.43a$. In this process, Si is consumed to form SiO_2. The volume of Si consumed is the annulus with the outer radius r_c and the inner radius r_b. Since Si is consumed, the effective dielectric value of the medium will decrease. The effect of Si consumption on the band gap is equivalent to etching out the Si annulus. If Si annulus is etched out the resultant structure will consist of air holes with radius $0.43a$. The upper and lower bands of this structure 2 are shown in Fig.3. 2. The difference in the band gap of the two structures: one with air hole radius 0.42a and the other with air hole radius 0.43a is calculated as the change in band gap due to Si consumption.

In the oxidation process, SiO_2 is formed simultaneously as Si is consumed which is replaced by SiO_2 rather than air. When the consumed Si annulus is replaced by SiO_2, the structure will consist of air hole radius $r_a = r_b = 0.42a$ and the Si/SiO_2 interface $r_c = 0.43a$. The upper and lower bands of the band gap of structure 3 can also be seen in Fig. 3.2. The difference in the band gap of structure 2 and structure 3 is calculated as the change in band gap due to SiO_2 formation. In practice, the oxide layer not only grows inside Si; it also expands towards the center, thereby shrinking the air hole. This, of course, is due to the fact that volume ratio of consumed Si to grown SiO_2 is 0.44. This effect is disregarded in [32]. To account for this phenomenon, the final air hole radius is carefully calculated as described in section 3.1. If the PC with original air hole radius $0.42a$ is oxidized until the radius of the Si/SiO_2 interface becomes $0.43a$, the final air hole radius will be $0.4069a$. This is the structure at the end point of oxidation and it is referred to as structure 4 in Fig. 3.2.

The absolute band gap and its upper and lower band edge values for structures1 through 4 are tabulated in Table 3.1. The corresponding contribution from each component of the oxidation process is shown in Table 3. 2. The overall change in band gap due to oxidation is 0.0055 normalized frequency. This results from the combined effect of increasing the band gap due to reduced Si filling ratio, and reducing band gap due to the increased filling ratio of SiO_2 that is replacing air.

Table 3.1. The band edge and band gap values for each structure in Fig. 3.2.(Air cylinder)

	Lower Band Edge	Upper Band Edge	Band Gap
Structure 1 (starting point)	0.3695	0.383	0.0135
Structure 2	0.3778	0.3985	0.0207
Structure 3	0.3770	0.397	0.0200
Structure 4 (end point)	0.3760	0.395	0.0190

Table 3.2. Contribution to band gap change from each component of the oxidization process (Air cylinder)

Structure 1 to Structure 4	0.0055 (change in band gap between starting point and end point)
Structure 1 to Structure 2	0.0072 (change in band gap when silicon is consumed)
Structure 2 to Structure 3	-0.0007(change in band gap when consumed Si is replaced by SiO_2)
Structure 3 to Structure 4	-0.001 (change in band gap when the air hole shrinks due to SiO_2 expansion)
Total change	0.0055

3.2.1 Change in band gap vs. oxide thickness

(a) Oxidation

Next, to analyze the dynamic nature of the contribution to band gap change from each component of the composite structure, a triangular lattice of air holes in Si is modeled again and the TE band gap is calculated for various oxide thicknesses as the oxide grows. The original air hole radius r_a is $0.35a$. The PC is oxidized until the oxide thickness of $0.2a$ is grown. This is the maximum oxide thickness that can be grown without closing the air hole entirely and maintaining the Si-SiO_2 interface within the unit cell. At these radii parameters, the structure does not have a TM band gap. Change in band gap due to each of the three components of the process: (i) Si consumption, (ii) SiO_2 formation, and (iii) air hole shrinkage is calculated, and their sum adds up to the overall change in band gap. The results are shown in Fig. 3.3.

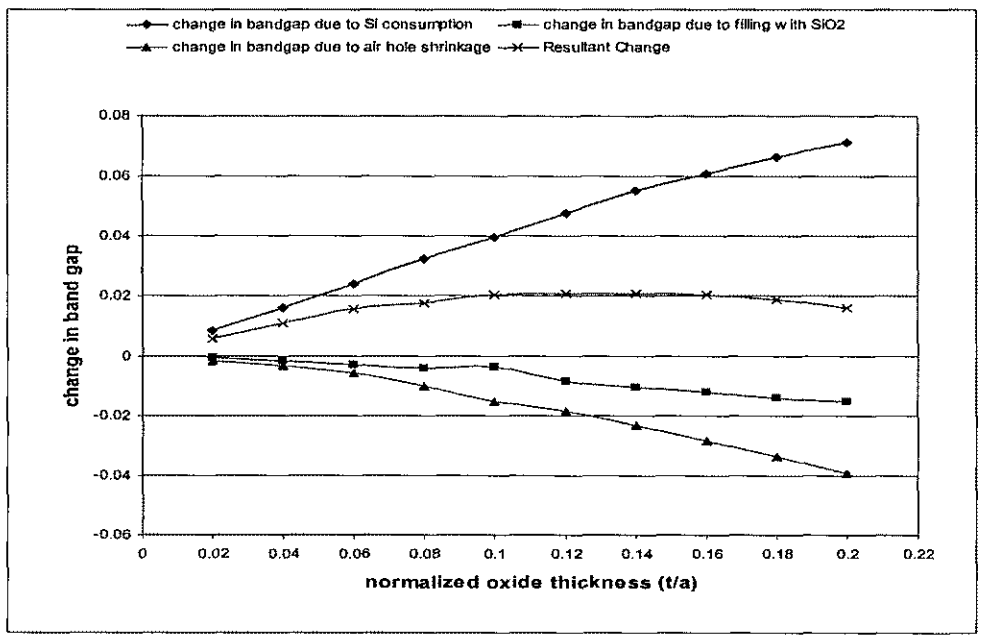

Fig.3.3. The TE band gap change due to Si consumption (—◆—) is positive and the band gap changes due to SiO_2 formation (—■—) and air hole shrinkage (—▲—) are negative. The resultant change (—×—) is found to be the sum of the three components.

As shown in Fig. 3.3, the change in band gap due to Si consumption is positive as the effective dielectric constant decreases as more and more Si is consumed. The band gap change due to SiO_2 filling as well as air hole shrinkage has negative values. Hence, the overall band gap change, the green curve (—×—) has a maximum at the oxide thickness of $0.14a$.

(b) Oxide etching

The effect of etching the oxide grown on the Si PC described above is also analyzed. At the end of the oxidation process, the oxide grown can be etched at a high selectivity without changing the dimensions of silicon. As the SiO_2 is etched, the air hole radius will increase. As a result, the effective dielectric constant will decrease thereby broadening the band gap. It is interesting to compare the effect of oxide growth with oxide etching. The evolution of the TE gap map is depicted in Fig. 3.4 (a) and (b), for the two processes. For each process, the gap map variation follows different paths and the final positions are different. Thus, the band gap engineering can be performed by oxidation and/or etching for the range of values shown in Fig. 3.4.

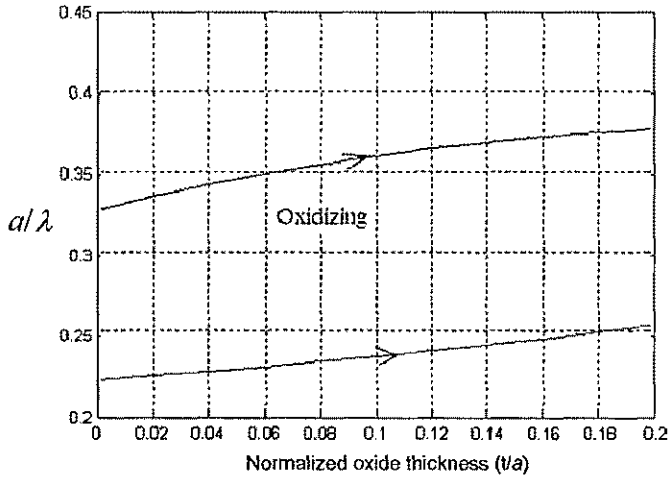

(a)

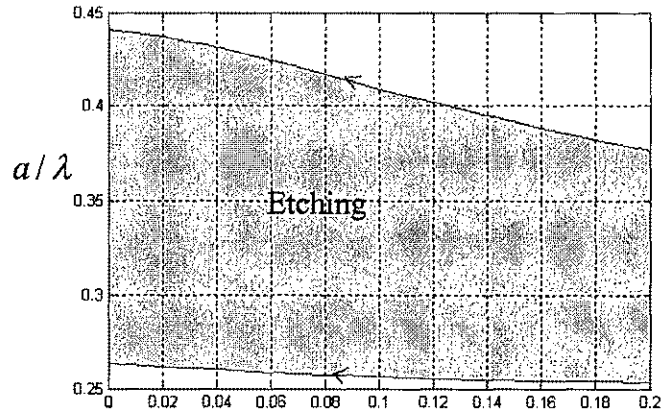

(b)

Fig. 3. 4. TE gap maps vs. oxide thickness (a) during oxidation (b) during etching.

(c) Oxidation and Partial Oxide Etching

Prior to oxidation an absolute band gap exists only for the air hole radius range (0.405-0.433)*a*; see Fig. 3.5 (a). We modeled the process in which the silicon around the air hole is oxidized until the outer radius of silicon dioxide reaches the maximum allowable value of 0.433a. The expanded volume of silicon dioxide is etched so that the air hole radius returns to the original value before oxidation. After oxidation and etching,

the band gap begins to appear at an air hole radius of 0.2a and continues to exist until the radius of 0.433a; see Fig. 3.5 (b).

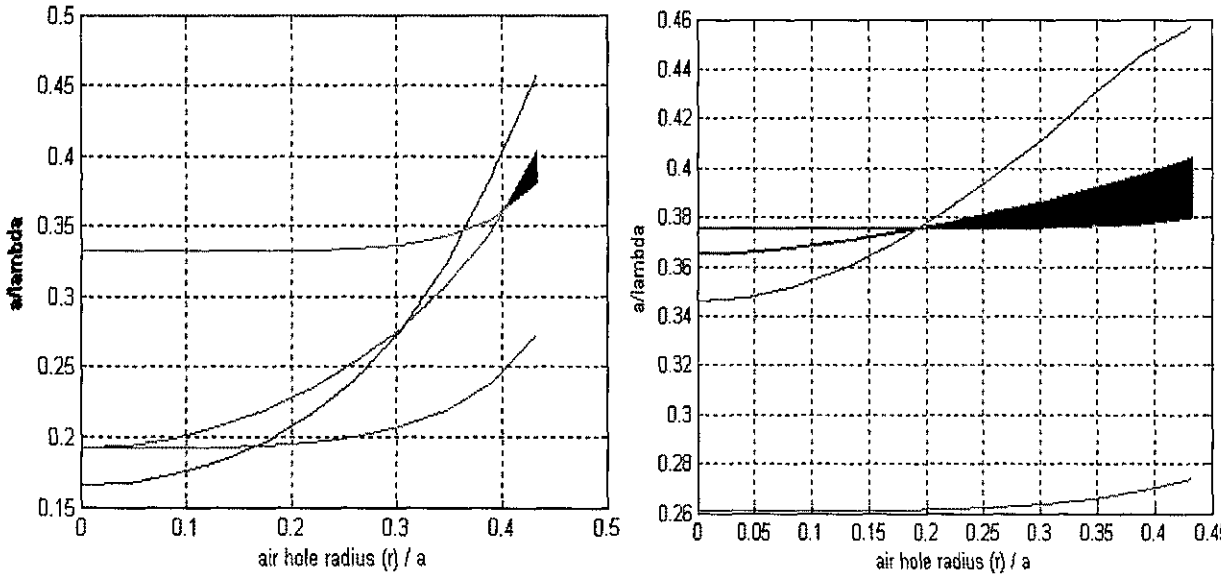

(a) (b)

Fig. 3.5. **(a)** Before oxidation, an absolute gap is formed starting from the air hole radius of 0.405a. **(b)**After oxidation and partial oxide etching, absolute band gap appears at the air hole radius of 0.2a.

4.3 Proposed Applications

(a)Heterostructure with large band gap

Large photonic band gaps are desirable in many applications. One way to enlarge the photonic band gap is to use multiple PC's together [39]. For silicon PC, although we can do this by etching a silicon substrate with different r_a/a ratio, local oxidation or selective oxidation provides another means of increasing the width of the band gap to make a monolithic device. If we grow an oxide layer with thickness t = 0.07a, the absolute band gap can be moved from (0.397-0.438) to (0.435-0.503). If we perform selective

oxidation on the original Si PC, a heterostructure can be produced as shown in Fig. 3.6. The width of the gap increases ~2.5 times. This structure will prevent the transmission of both TE and TM polarized wave within a much larger range.

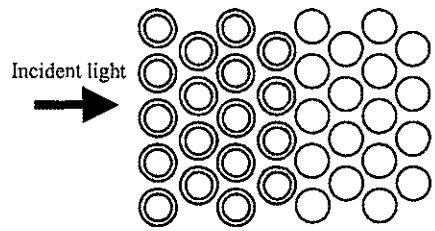

Fig. 3.6. Schematic diagram showing the oxidized heterostructure with larger PBG. The annulus represents the oxide layer and black empty circle stands for the air hole.

(b)Large cavity

Oxidizing a small center region of the original silicon PC will form another structure with a different band gap position, as shown in Fig. 3.7 (a) and (b) for a triangular lattice. As noted above, the lower edge of the TE band gap will move up with the oxidation. Therefore, the lower band-gap edge of the TE mode will eventually fall into the band gap of the un-oxidized silicon PC that is surrounding the oxidized PC. The low-edge mode at the J point will have very small loss and zero group velocity for the ideal PC. This may make it easier to create a white-light source and multiple wavelength-mixing. The small group velocity will elongate the interaction period with the center region. With active material introduced into the center edge-mode region, lasing action will be facilitated by the properties of low loss and low group velocity. A similar structure can be formed by etching more of the center region than the outside, and a photonic crystal laser has been reported in InP by embedding quantum wells into the center [40]. In the case of Si PC,

an identical structure can be produced by etching off the oxide in Fig. 3.7 (a) and embedding similar quantum wells.

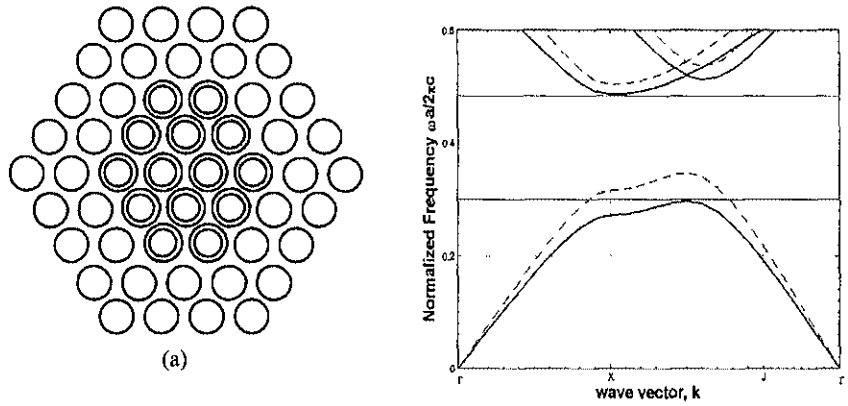

Fig. 3.7 (a). Schematic diagram of a heterostructure for large cavities. The center region is the oxidized triangular lattice. (b) Comparison of the dispersion curves for the structures: un-oxidized (solid line) and oxidized (dashed line).

CHAPTER IV

EFFECT OF OXIDATION AND OXIDE ETCHING ON THE PHOTONIC BAND GAP: SILICON CYLINDERS EMBEDDED IN AIR

4.1 Calculation of the radius parameters during oxidation

In this chapter results of the analysis of the structure consisting of Si cylinders embedded in air background are presented. In such a structure a broad TM band gap can be obtained for a wide range of radius parameters. Applications of such pillar arrays have been demonstrated in enhancement of light extraction [41] and wave guiding [42]. When the Si cylinder is oxidized, several processes occur in the structure: (i) Si is consumed and the Si radius shrinks from the original radius, (ii) SiO_2 is formed in the place of consumed Si, (iii) the outer radius of SiO_2 exceeds the original Si radius because of SiO_2 volume expansion. The end result at the termination of oxidation will be as shown in Fig. 4.1. Calculation of radius parameters is similar to the structure presented in Chapter 3.

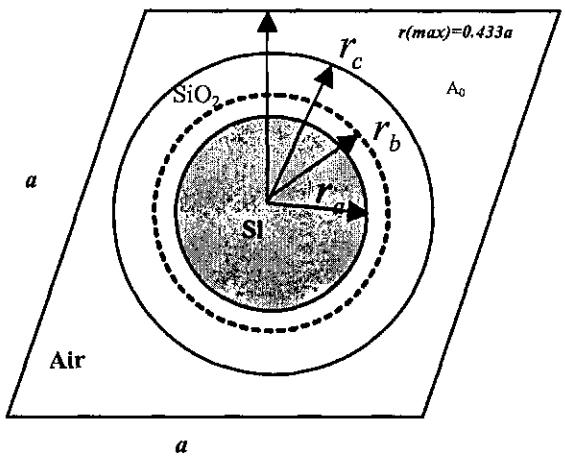

r_a: radius of Si after oxidation,
r_b: radius of Si before oxidation,
r_c: SiO_2 outer radius
ε_a: permittivity of the air 1,
ε_b: permittivity of SiO_2 2.09,
ε_c: permittivity of silicon 12.08, and
A_0: the area of the unit cell.

Fig. 4.1 Oxidized Si cylinder in a unit cell of triangular lattice.

$$\frac{\pi r_b^{\,2} - \pi r_a^{\,2}}{\pi r_c^{\,2} - \pi r_a^{\,2}} = 0.44 \tag{4.1}$$

By defining the thickness of the oxide layer t as

$$t = r_c - r_a \tag{4.2}$$

we obtain:

$$r_a = -0.44t + \sqrt{r_b^{\,2} - 0.2464t^2} \tag{4.3}$$

$$r_c = 0.56t + \sqrt{r_b^{\,2} - 0.2464t^2} \tag{4.4}$$

4.2 Results and Discussion

The specific structure we modeled has the following parameters: the original radius of Si cylinder before oxidation, r_b =0.28a; the cylinders are oxidized until the radius of Si/SiO_2 interface, r_a , becomes 0.1a. At that point, the outer radius of SiO_2, r_c will be 0.405a. PC's where higher dielectric constant atoms are embedded in lower dielectric medium tend to support TM band gap and lack TE band gap and there is no absolute band gap. Therefore, our study is confined to TM band gap in this chapter. The upper and lower bands of the TM band gap are shown in Fig. 4.2. Structure 1 represents the original structure before oxidation. Structure 2 represents the structure when Si is consumed. Structure 3 represents the structure when SiO_2 is formed in the place of consumed Si. Structure 4 represents the structure when air is displaced by the expanded volume of SiO_2.

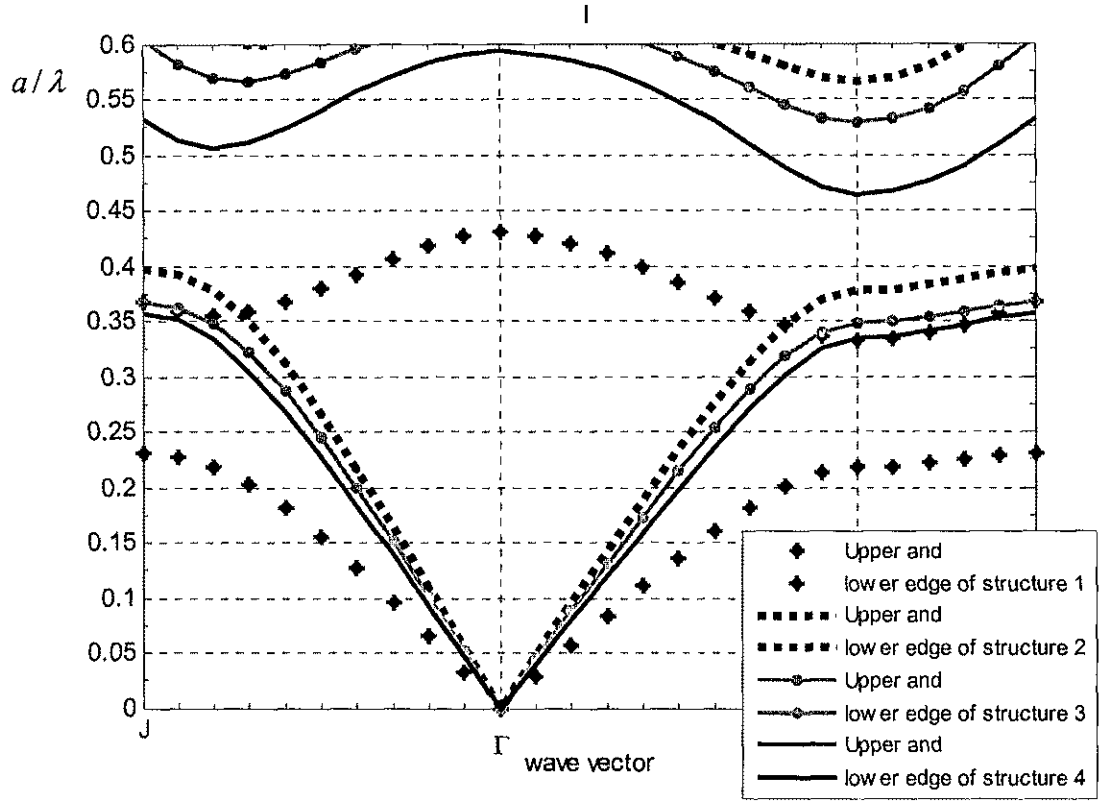

Fig. 4.2 TM dispersion curves for the structure consisting of Si cylinders in air background. structure 1: when the Si atom radius is 0.28*a*, structure 2: when Si is consumed and Si atom radius becomes 0.1a, structure 3: when consumed Si is replaced by SiO2, structure 4: When outer radius of the atom becomes larger than the original atom radius due to silicon dioxide volume expansion.

Table 4.1. The band edge and band gap values for each structure in Figure 4.2.(Si cylinder)

	Lower Band Edge	Upper Band Edge	Band Gap
Structure 1 (starting point)	0.2303	0.333	0.1027
Structure 2	0.397	0.5657	0.1687
Structure 3	0.3669	0.5284	0.1615
Structure 4 (end point)	0.3566	0.4638	0.1072

Table 4.2 Contribution to band gap change from each component of the oxidization process (Si cylinder).

Structure 1 to Structure 4	0.0045 (change in band gap between starting point and end point)
Structure 1 to Structure 2	0.066(change in band gap due to silicon consumption)
Structure 2 to Structure 3	-0.0072(change in band gap when consumed Si is replaced by SiO_2)
Structure 3 to Structure 4	-0.0543 (change in band gap due to SiO_2 volume expansion)
Total change	0.0045

4.2.1 Change in band gap vs. oxide thickness

(a) Oxidation

Next, to analyze the dynamic nature of the contribution to band gap change from each of the three components, Si consumption, SiO_2 formation, and SiO_2 volume expansion, the TM band gap is calculated for various oxide thicknesses as the oxide grows. The results are shown in Fig. 4.3. As mentioned above, at the end of oxidation, the radius of Si/SiO_2 interface is $0.1a$, the outer radius of SiO_2 is $0.405a$ and the oxide thickness is $0.3a$. Oxidation beyond this point is not recommended because it can drastically reduce the mechanical strength of the structure. In the structure modeled above, the TM band gap exists for a wide range of oxide thicknesses from 0 to $0.3a$. Since this structure allows us to analyze the band gap for a wider range of oxide thicknesses than in the case of the air cylinder PC presented in Chapter III, the non-linear nature of the band gap change due to the three components of oxidation is more clearly seen. Maximum band gap change occurs at the oxide thickness of $0.21a$.

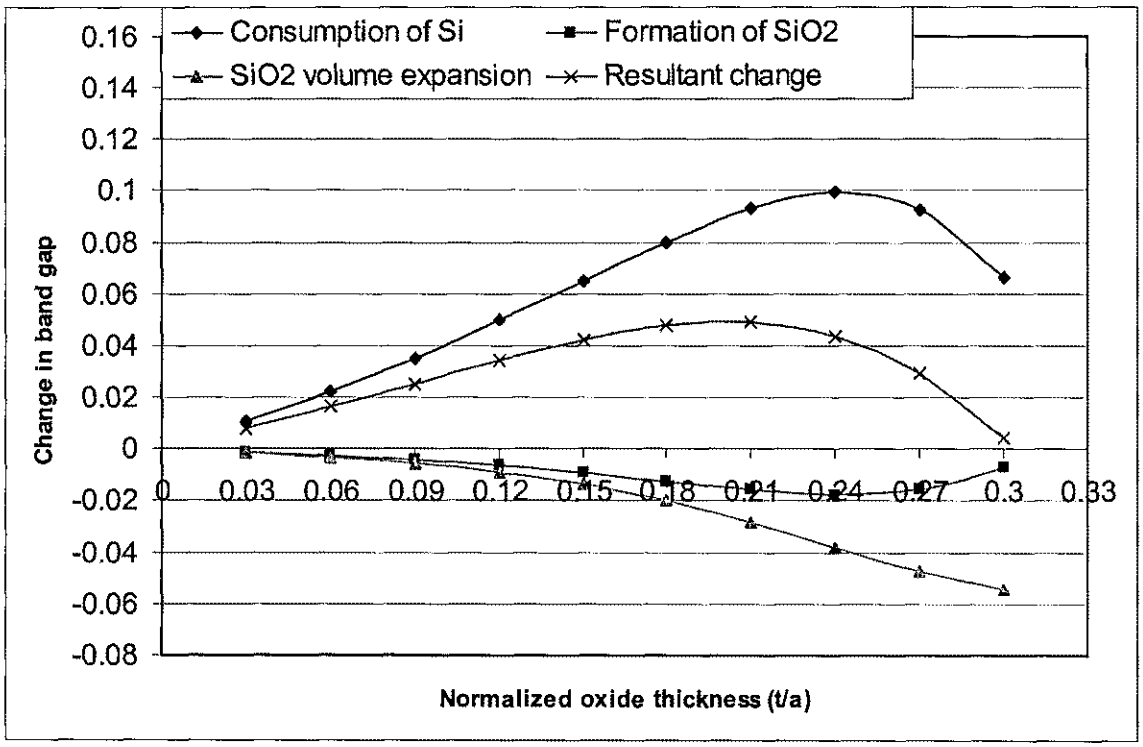

Fig. 4.3. The TM band gap change due to Si consumption (—◆—) is positive and the band gap changes due to SiO_2 formation (—■—) and SiO_2 volume expansion(—▲—) are negative. The resultant change (—×—) is found to be the sum of the three components.

(b) Etching

At the end of oxidation, silicon dioxide can be etched without affecting Si dimensions. Since etching silicon dioxide will decrease the effective dielectric constant of the PC, it broadens the band gap and shifts the band gap position upward. However, since the dielectric constant of silicon dioxide is much smaller than that of silicon, the effective dielectric constant will change slowly with the thickness of etched oxide. At the starting point of oxidation, the Si radius of $0.28a$ and the band gap is found to be (0.2303-0.333). At the end of oxidation the band gap moves up to (0.3566-0.4638). Subsequently, when the grown oxide is etched, the band gap moves farther up, and at the end of the etching process it was found to be (0.4080-0.5680). The Si radius at the end of etching will be

smaller than the Si radius before oxidation because Si has been consumed during oxidation. During the oxide etching process, the band gap value can be tuned between 0.1 and 0.16 for the midgap frequencies ranging from 0.41 to 0.49. The gap map during oxidation and oxide etching are compared in Fig. 4.4.

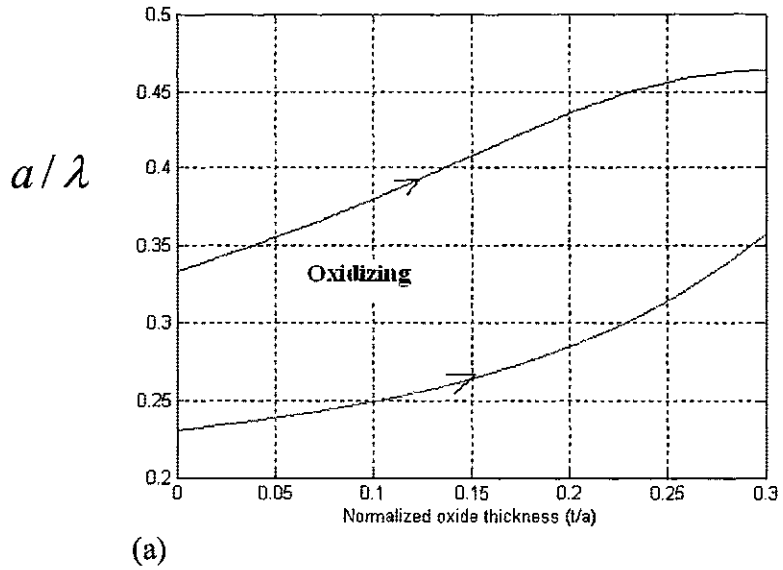

(a)

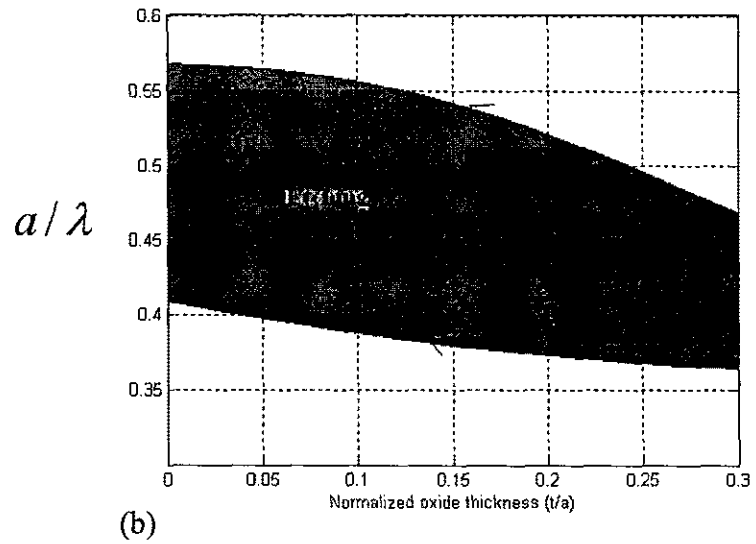

(b)

Fig. 4. 4. TM gap maps vs. oxide thickness (a) during oxidation and (b) during etching.

4.3 Proposed Application

Single Defect Cavity

When disorder or defects are introduced in the periodic dielectric structure of a photonic crystal, the light modes can appear within the band gap. Since these light modes are highly localized around the defect, a microcavity in the size of a few optical wavelengths can be formed. Constructing optical microcavities with small mode volume and large quality factor is one of the most studied topics of PC due to their applications such as ultra-low threshold lasers, enhanced or suppressed spontaneous emission and microscale optical filters. In a structure consisting of silicon cylinders of radius $0.28a$ in air, when the center cylinder is oxidized up to the oxide thickness of $0.15a$, leaving the rest of the cylinders untouched, a defect mode appears inside the band gap due to the upset in symmetry. See Fig. 4.5 (a) and (b).

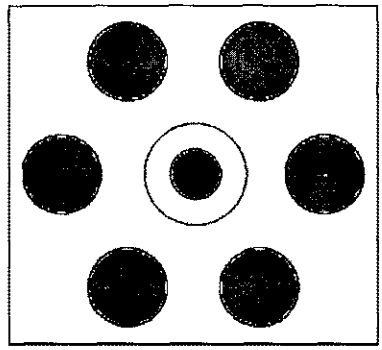

(a)

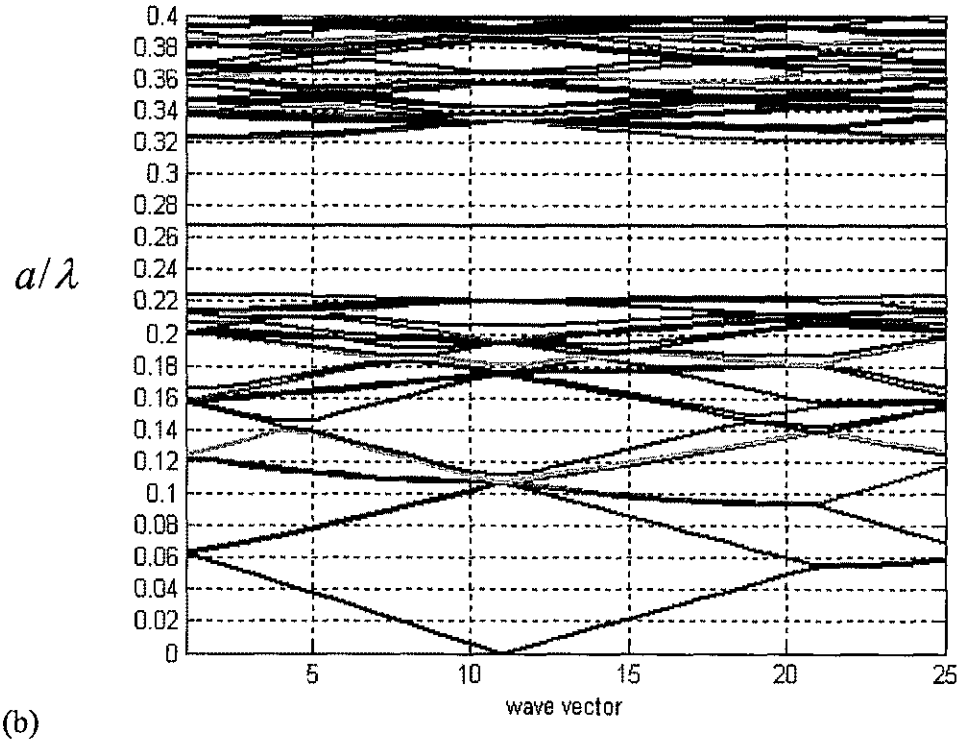

(b)

Fig. 4.5 (a) A single defect formed by oxidizing the center atom in a Si cylinder PC (b) The defect mode is found at (0.2696) inside the band gap (0.23~0.33) for the oxide thickness of $0.3a$

The defect frequency is found to depend strongly on the oxide thickness. Therefore, in such a structure, the defect frequency can be tuned by varying the oxide thickness. When the oxide thickness is $0.15a$, the defect mode starts to appear at 0.2317 normalized frequency. See Fig. 4.6. As the oxide grows, the defect shifts to higher frequencies and when the oxide thickness is $0.3a$, the defect mode is found at the normalized frequency value of 0.2696. When the grown oxide is etched, the defect frequency shifts farther upward and reaches 0.2984 when all the oxide is removed.

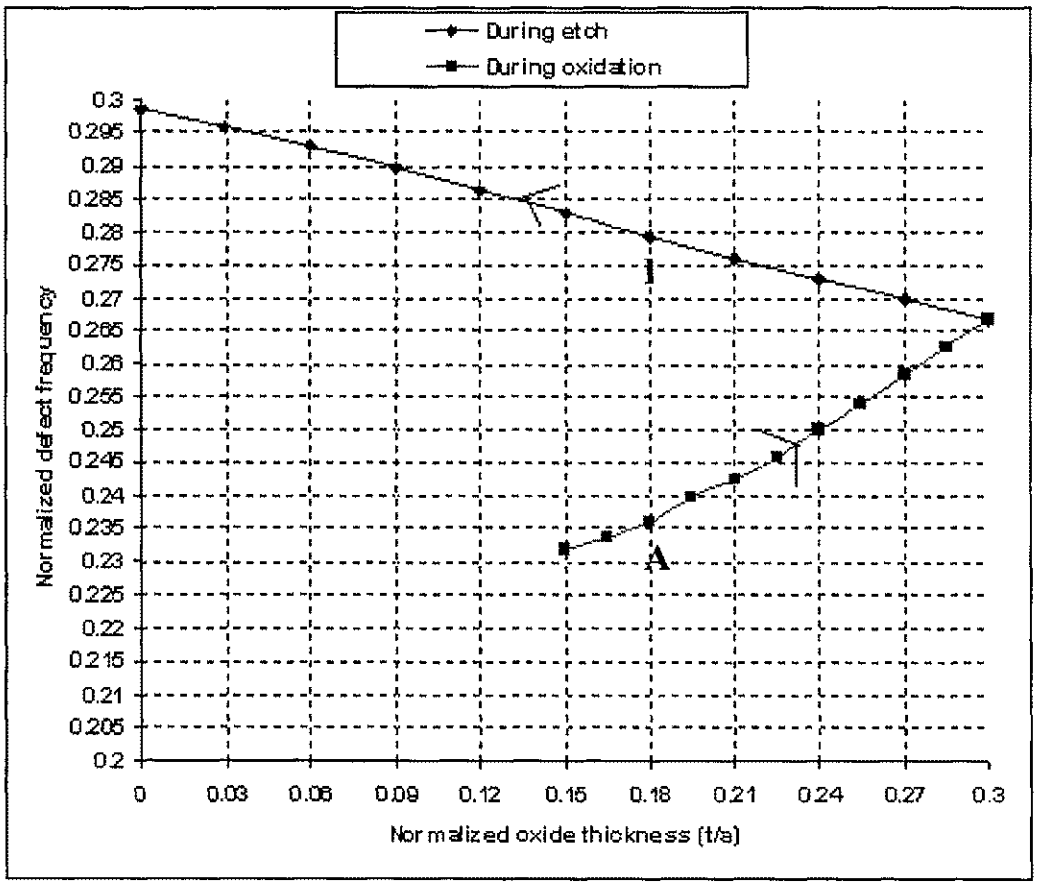

Fig. 4.6 The defect mode starts to appear when oxide thickness reaches $0.15a$ and shifts upward as the oxide grows. No defect mode was found for thinner oxide thickness.

An interesting fact observed here is that for the same oxide thickness around the Si cylinder the defect frequency value will be different during oxidation and etching. For instance, take points A and B; oxide thickness around the cylinder is 0.18a for both A and B. However, the defect frequencies are different. Point A is on the oxidation path, and it has larger Si dimensions. Point B is on the etching path, and it will have smaller Si dimensions since it has returned from the end point of oxidation.

CHAPTER V

SUMMARY AND FUTURE WORK

A thorough analysis of the effects of oxidation and oxide etching on the photonic band structure of silicon PC's has been presented. Two structures have been modeled: (i) air cylinders embedded in a silicon background and (ii) silicon cylinders embedded in an air background. The plane wave expansion method has been employed to model the structures. The results have been obtained for each structure consisting of triangular lattice.

During oxidation three processes occur simultaneously: silicon is consumed, consumed silicon is replaced by silicon dioxide, and silicon dioxide dimensions exceed the original silicon dimensions, thereby displacing air. The contribution of each component to the change in photonic band gap is analyzed at various oxide thickness and the results were presented. In both structures (i) and (ii), the band gap is broadened and shifted up towards higher frequencies as the oxide grows. However, this is not a linear process; in each structure there is an oxide thickness value that gives rise to maximum change in the band gap. This phenomenon is explained in terms of contributions from each component of the oxidation process. Consumption of silicon causes the band gap to broaden; the band gap change due to this component is therefore positive. Replacement of consumed silicon by silicon dioxide and the volume expansion of silicon dioxide cause the band gap to narrow. Hence, the band gap change due to these two components is negative. The positive and negative effects compete with each other giving rise to the resultant change in band gap.

The effect of etching the oxide grown on the Si PC was also analyzed for each structure. At the end of the oxidation process, the oxide grown can be etched at a high selectivity without changing the dimensions of silicon. When the oxide is etched, the effective dielectric constant will decrease thereby broadening the band gap. The gap map variation follows different paths for oxidation and etching processes and the final positions are different. Thus, the band gap engineering can be performed by oxidation and/or etching.

Possible applications are proposed for both structures. For air cylinders in a silicon background, a heterogeneous photonic crystal of enlarged band gap and a large cavity for band edge mode confinement can be produced by localized oxidation. For silicon cylinders in an air background, a single defect cavity can be introduced by localized oxidation and defect frequency can be tuned by varying the oxide thickness by oxidation and/or etching.

These results were presented at several conferences: Optics in the Southeast, September 2006 in Charlotte, North Carolina; 73rd annual meeting of SEAPS, November 2006 in Williamsburg, Virginia; and the MRS Fall meeting, November 2006 in Boston, Massachusetts. The results were also published in the proceedings of Material Research Society and submitted to Optics Express [43,44].

Future work includes, but is not limited to, changing the refractive index of silicon by optical absorbing pulses to create a dynamic photonic crystal.

APPENDIX I

MATHEMATICAL DERIVATION OF PLANE WAVE EXPANSION METHOD

Fourier series representation of electric permittivity and magnetic permeability functions:

$$\frac{1}{\varepsilon(r)} = \sum_{\vec{G}} u_{\vec{k}}(\vec{G}).e^{j\vec{G}.\vec{r}} \tag{A.1}$$

$$\mu(r) = \sum_{\vec{G}} \eta(\vec{G}).e^{j\vec{G}.\vec{r}} \tag{A.2}$$

Fourier series representation of EM field:

$$\overline{H} = \sum_{\vec{G}} \sum_{\lambda} \overline{e}^{\lambda} h(\vec{G})\, e^{j(\vec{k}+\vec{G}).\vec{r}} \tag{A.3}$$

The Helmholtz equation:

$$\nabla \times \frac{1}{\varepsilon(r)} \nabla \times \overline{H} = \frac{\omega^2}{c^2} \mu.\overline{H} \tag{A.4}$$

Constructing the L.H.S of the Helmholtz equation:

$$\nabla \times \overline{H} = j.\sum_{G} \sum_{\lambda}^{2} h(\vec{G})(\vec{k}+\vec{G}) \times \overline{e}^{\lambda} e^{j(\vec{k}+\vec{G}).\vec{r}} \tag{A.5}$$

by multiplying with $\frac{1}{\varepsilon(r)} = \sum_{\vec{G}} u_{\vec{k}}(\vec{G}).e^{j\vec{G}.\vec{r}}$ and by replacing the index $\vec{G}$ in this series

with $\vec{G}'$. Therefore, (A.5) becomes

$$\frac{1}{\varepsilon(r)}.\nabla\times\overline{H}=j.\sum_{G'}\sum_{G}\sum_{\lambda}^{2}h(\vec{G}).u_{k}^{-}(\vec{G'})(\vec{k}+\vec{G})\times\overline{e}^{\lambda}.e^{j(\vec{k}.+\vec{G}+\vec{G'}).\vec{r}} \tag{A.6}$$

$$\nabla\times\frac{1}{\varepsilon(r)}.\nabla\times\overline{H}=-.\sum_{G'}\sum_{G}\sum_{\lambda}^{2}h(\vec{G}).u_{k}^{-}(\vec{G'})\left\{(\vec{k}+\vec{G}+\vec{G'})\times(\vec{k}+\vec{G})\times\overline{e}^{\lambda}\right\}e^{j(\vec{k}.+\vec{G}+\vec{G'}).\vec{r}} \tag{A.7}$$

Above is the lefthand side of the wave equation, (A.4). Now we will construct the righthand side of the wave equation.

$$\frac{\omega^{2}}{c^{2}}.\mu.\overline{H}=\frac{\omega^{2}}{c^{2}}.\sum_{\vec{G'}}\sum_{\vec{G}}\sum_{\lambda}^{2}\eta(\vec{G'}).h(\vec{G})\overline{e}^{\lambda}e^{j(\vec{k}+\vec{G}+\vec{G'}).\vec{r}} \tag{A.8}$$

Therefore, the wave equation (A.4) becomes,

$$-.\sum_{G}\sum_{G}\sum_{\lambda}^{2}h(\vec{G}).u_{k}^{-}(\vec{G})\left\{(\vec{k}+\vec{G}+\vec{G'})\times(\vec{k}+\vec{G})\times\overline{e}^{\lambda}\right\}e^{j(\vec{k}.+\vec{G}+\vec{G})\vec{r}}=\frac{\omega^{2}}{c^{2}}.\sum_{\vec{G}}\sum_{\vec{G}}\sum_{\lambda}^{2}\eta(\vec{G'})h(\vec{G})\overline{e}^{\lambda}e^{j(\vec{k}+\vec{G}+\vec{G})\vec{r}} \tag{A.9}$$

The outermost summations $\sum_{G'}$ on each side of (A.9) are linear combinations of various independent wave functions $e^{j(\vec{k}.+\vec{G}+\vec{G'}).\vec{r}}$. Therefore we can equate each coefficient term by term, which enables us to strip off the outermost summations on both sides and the equation becomes,

$$-\sum_{G}\sum_{\lambda}^{2} h(\vec{G}).u_k(\vec{G})\left\{(\vec{k}+\vec{G}+\vec{G})\times(\vec{k}+\vec{G})\times\vec{e}^{\lambda}\right\}e^{j(\vec{k}+\vec{G}+\vec{G})\vec{r}}=\frac{\omega^2}{c^2}\cdot\sum_{\vec{G}}\sum_{\lambda}^{2}\eta(\vec{G}).h(\vec{G})\vec{e}^{\lambda}e^{j(\vec{k}+\vec{G}+\vec{G})\vec{r}} \quad \text{(A.10)}$$

$$-\sum_{G}\sum_{\lambda}^{2} h(\vec{G}).u_k(\vec{G}')\left\{(\vec{k}+\vec{G}+\vec{G}')\times(\vec{k}+\vec{G})\times\vec{e}^{\lambda}\right\}=\frac{\omega^2}{c^2}\sum_{\vec{G}}\sum_{\lambda}^{2}\eta(\vec{G}').h(\vec{G})\vec{e}^{\lambda} \quad \text{(A.11)}$$

Here, the index $\vec{G}$ serves as the summation index and $\vec{G}'$ is a free index. As far as the summation is concerned, $\vec{G}'$ is just a constant. We can define, $\vec{G}''=\vec{G}+\vec{G}'$,which gives $\vec{G}'=\vec{G}''-\vec{G}$. Therefore, (A.4) becomes,

$$-\sum_{G}\sum_{\lambda}^{2} h(\vec{G}).u_k(\vec{G}''-\vec{G})\left\{(\vec{k}+\vec{G}'')\times(\vec{k}+\vec{G})\times\vec{e}^{\lambda}\right\}=\frac{\omega^2}{c^2}\sum_{\vec{G}}\sum_{\lambda}^{2}\eta(\vec{G}''-\vec{G}).h(\vec{G})\vec{e}^{\lambda} \quad \text{(A.12)}$$

We can simplify the triple vector product as follows:

$$\{(\vec{k}+\vec{G}')\times(\vec{k}+\vec{G})\times\vec{e}^{\lambda}\}\bullet\vec{e}^{\lambda'}=\{\vec{e}^{\lambda'}\times(\vec{k}+\vec{G}')\}\bullet\{(\vec{k}+\vec{G})\times\vec{e}^{\lambda}\}=-\{(\vec{k}+\vec{G}').\times\vec{e}^{\lambda'}\}\bullet\{(\vec{k}+\vec{G})\times\vec{e}^{\lambda}\} \quad \text{(A.13)}$$

Therefore, by substituting (A.13) in (A.12) we can obtain

$$\sum_{\vec{G}}\sum_{\lambda}h(\vec{G})u_k(\vec{G}'-\vec{G})\left\|(\vec{k}+\vec{G}')\right\|(\vec{k}+\vec{G})\left\|\{(\vec{e}^{3}\times\vec{e}^{\lambda})\bullet(\vec{e}^{3}\times\vec{e}^{\lambda}')\}=\frac{\omega^2}{c^2}\sum_{\vec{G}}\sum_{\lambda}\eta(\vec{G}'-\vec{G})h(\vec{G})(\vec{e}^{\lambda}\bullet\vec{e}^{\lambda})\right. \quad \text{(A.14)}$$

In (A.14) it can be seen that the operator Θ operating on $h(\vec{G})$ is equal to a constant value times $h(\vec{G})$, where $\Theta=u_k(\vec{G}''-\vec{G})\left\|(\vec{k}+\vec{G}'')\right\|(\vec{k}+\vec{G})\left\|\{(\vec{e}^{3}\times\vec{e}^{\lambda})\bullet(\vec{e}^{3}\times\vec{e}^{\lambda}')\right.\}$

Therefore (A.14) constitutes an eigenvalue problem and the operator Θ can be represented in matrix form as in (A.15).

$$\Theta = u_k(\vec{G}' - \vec{G})\left\|(\vec{k}+\vec{G}')\right\|(\vec{k}+\vec{G})\left\|\{(\hat{e}^{3}\times\hat{e}^{\lambda})\bullet(\hat{e}^{3}\times\hat{e}^{\lambda'})\}\right. = u_k(\vec{G}' - \vec{G})\left\|(\vec{k}+\vec{G}')\right\|(\vec{k}+\vec{G})\left\|\begin{pmatrix} \hat{e}^{2}\bullet\hat{e}^{2'} & -\hat{e}^{2}\bullet\hat{e}^{1'} \\ -\hat{e}^{1}\bullet\hat{e}^{2'} & \hat{e}^{1}\bullet\hat{e}^{1'} \end{pmatrix}\right. \quad \text{(A.15)}$$

REFERENCES

1. E. Yablonovitch, Phys. Rev. Lett. **58**, 2059 (1987).
2. S. Y. Lin, J. G. Fleming, D. L. Hetherington, B. K. Smith, R. Biswas, K. M. Ho, M. M. Sigalas, W. Zubrzycki, S. R. Kurtz, and J. Bur, Nature **394**, 251 (1998).
3. S. Y. Lin, E. Chow, S. G. Johnson, and J. D. Joannopoulos, Opt. Lett. **25**, 1297 (2000).
4. K. Busch and S. John, Phys. Rev. E **58**, 3896 (1998).
5. U. Gruning, V. Lehmann, S. Ottow, and K. Busch, Appl. Phys. Lett. **68**, 747 (1996).
6. J. D. Joannopoulos, R. D. Meade and J. N. Winn, Photonic Crystals, (Princeton University Press, Princeton, 1995).
7. S. Noda, K. Tomoda, N. Yamamoto, and A. Chutinan, Science, **289**, 604 (2000).
8. K. Inoue, M. Wada, K. Sakoda, A. Ymanaka, M. Hayashi and J. W. Haus, Jpn. J. Appl. Phys. **33**, L1463 (1994).
9. K. Ohtaka, Phys. Rev. **B19**, 5057 (1979).
10. K. Ohtaka and M. Inoue, Phys. Rev. **B25**, 677 (1982).
11. T. Holland, C. E. Blanford, and A. Stein, Science **281**, 538 (1998).
12. S. John, Phys. Rev. Lett. **58**, 2486 (1987).
13. W. S. Bigelow and E. G. Farr,Ultra-Wideband Short-Pulse Electromagnetics 4, 231 (1998).
14. P.I. Borel, L.H. Frandsen, A. Harpøth, J.B. Leon, H. Liu, M. Kristensen, W. Bogaerts, P. Dumon, R. Baets, V. Wiaux, J. Wouters and S. Beckx, Electron. Lett. **40,** 1263 (2004).
15. S. Fan, S. G. Johnson, J. D. Joannopoulos, C. Manolatou, and H. A. Haus, J.Opt. Soc. Am. **B18,** 162 (2001).
16. Y. Sugimoto, N. Ikeda, N. Carlsson, K. Asakawa, N. Kawai and K. Inoue, Opt. Lett., **2**, 388 (2002).
17. S. Lin, E. Chow, J. Bur, S. G. Johnson, and J. D. Joannopoulos, Opt. Lett. **27**, 1400 (2002).
18. S. Boscolo, M. Midrio and T. F. Krauss, Opt. Lett. **27**, 1001 (2002).
19. A. Yariv, Y. Xu, and R. K. Lee and A. Scherer, Opt. Lett. **24**, 711 (1999).
20. J. K. Knight, J. Broeng, T. A. Birks, and P. St. J. Russell, Science, **282**, 1476 (1998).
21. O. Painter, R. K. Lee, A. Scherer, A. Yariv, J. D. O'Brien, P. D. Dapkus, and I. Kim, Science **284**, 1819 (1999).
22. M. Imada, S. Noda, A. Chutinam, T. Tokuda, M. Murata, and G. Sasaki, appl. Phys. Lett. **75**, 316 (1999).
23. S. Noda, A. Chutinan, and M. Imada, Nature **407**, 608 (2000).
24. Y. Ohtera, T. Sato, T. Kawashima, T. Tamamura, and S. Kawakami, Electron. Lett. **35**, 12171 (1999).
25. A. Blanco, E. Chomski, S. Grabtchak, M. Ibisate, S. John, S. W. Leonard, C. Lopez, F. Meseguer, H. Miguez, J. P. Mondla, G. A. Ozin, O. Toader, and H. M. v. Driel, Nature **405**, 437 (2000).
26. M. Loncar, T. Doll, J. Vuckovic, and A. Scherer, Journal of Lightwave Technology **18**, 1402 (2000).

27. T. Geppert, J. Schilling, R. Wehrspohn, and U. Gosele, Silicon Photonics, Topics Appl. Phys. **94**, 295 (2004).
28. S. Guo and S. Albin, Opt. Expr. **11**, 167 (2003).
29. L. Liao, D. Samara-Rubio, M. Morse, A. Liu, D. Hodge, D. Rubin, U. D. Keil and T. Franck, Opt. Expr. **13**, 3129 (2005).
30. O. Boyraz & B. Jalali, Opt. Expr. **12**, 5269 (2004).
31. H. Rong, et al. Nature **433**, 292 (2005).
32. A. Glushko and L. Karachevtseva, Opto-electronics Rev. **14**, 202 (2006).
33. H. Ali, "Modeling and simulation of silicon photonic crystals : effect of oxidation and etching", Old Dominion University M.S. Thesis, Electrical Engineering(2005).
34. http://www.mtmi.vu.lt/pfk/funkc_darinia/quant_mech/bands.htm
35. http://ab-initio.mit.edu/photons/tutorial
36. S. Guo, "Photonic Crystals: Modeling and Simulation", Old Dominion University Ph. D. Dissertation, Electrical Engineering (2003).
37. F. Wu, "Modeling and Simulation of Photonic Crystal Fibers and Distributed Feedback Photonic Crystal Fiber Lasers", Ph. D. Dissertation, Electrical Engineering (2005).
38. S. M. Sze, S. M. Sze, Semiconductor Devices: Physics and Technology (John wiley & sons, Inc., 2001).
39. Qinghai Song, Liying Liu, Wencheng Wang, Lei Xu, Proc. of SPIE **5061**, 232, (2003).
40. S. Kwon, S. Kim, S. Kim, Y. Lee, and S. Kim, Opt. Express.**12**, 356 (2004).
41. T. Ba Ba, K. Inoshita, J. Yonekura, M. Ariga, A. Matsutani, T. Tiyamoto, F. Koyama and K. Iga, J. Lightwave Technol. **17**, 2113 (1999).
42. V. Poborchii, T. Tada and T. Kanayama, Opt. Communications. **210**, 285 (2002).
43. M. Thitsa, H. Ali, Feng Wu, K. Peters and S. Albin, "Modeling the Effect of Oxidation and Etching of Silicon Photonic Crystals", in *Multiscale Modeling of Materials,* edited by R. Devanathan, M. J. Caturla, A. Kubota, A. Chartier, S. Phillpot (Mater. Res. Soc. Symp. Proc. **978E**, Warrendale, PA, 2007), GG05-26.
44. M. Thitsa, F. Wu and Sacharia Albin, "Band gap engineering of silicon photonic crystals by oxidation and oxide etching", submitted to Opt. Expr. (2007).

VITA

Makhin Thitsa

Education:

B.S. (Electrical Engineering), Magna cum Laude 2005
Old Dominion University, Norfolk Virginia

M.S. (Electrical Engineering) May 2007
Old Dominion University, Norfolk Virginia

Publications

1. Makhin Thitsa, Haider Ali, Feng Wu, Kurt Peters and Sacharia Albin, "Modeling the Effect of Oxidation and Etching of Silicon Photonic Crystals", in *Multiscale Modeling of Materials,* edited by R. Devanathan, M. J. Caturla, A. Kubota, A. Chartier, S. Phillpot (Mater. Res. Soc. Symp. Proc. **978E**, Warrendale, PA, 2007), GG05-26.
2. Makhin Thitsa, Feng Wu and Sacharia Albin, "Band gap engineering of silicon photonic crystals by oxidation and oxide etching", submitted to Optics Express.(2007)

Conference Presentations

1. Makhin Thitsa, Feng Wu, and Sacharia Albin, "Optical Properties and Band Structures of Heterogeneous Photonic Crystals Formed by Localized Oxidation." Paper presented at Optics in the Southeast, September 6-8, 2006, Charlotte, North Carolina.

2. Makhin Thitsa and Sacharia Albin, "Tuning Silicon Photonic Crystal Band Gap by Oxidation and Etching." Paper presented at 73rd Annual Meeting of Southeastern Section of the American Physical Society (SESAPS), November 9-11, 2006, Williamsburg, Virginia.

3. Makhin Thitsa, Haider Ali, Feng Wu, Kurt Peters and Sacharia Albin, "Modeling the effect of oxidation and etching of silicon photonic crystals", Paper presented at MRS Fall Meeting, November 27-December 1, 2006, Boston Massachusetts.